PHYSICAL REVIEW E **83**, 056710 (2011)

Numerics of the lattice Boltzmann method: Effects of collision models on the lattice Boltzmann simulations

Li-Shi Luo (罗礼诗),[1,*] Wei Liao (廖伟),[1,†] Xingwang Chen (陈兴旺),[1] Yan Peng (彭艳),[1,‡] and Wei Zhang (张炜)[2,§]
[1]*Department of Mathematics & Statistics and Center for Computational Sciences Old Dominion University, Norfolk, Virginia 23529, USA*
[2]*Department of Fluid Machinery and Engineering, School of Energy and Power Engineering Xi'an Jiaotong University,*
Xi'an 710049, Shaanxi Province, People's Republic of China

(Received 11 January 2011; published 26 May 2011)

We conduct a comparative study to evaluate several lattice Boltzmann (LB) models for solving the near incompressible Navier-Stokes equations, including the lattice Boltzmann equation with the multiple-relaxation-time (MRT), the two-relaxation-time (TRT), the single-relaxation-time (SRT) collision models, and the entropic lattice Boltzmann equation (ELBE). The lid-driven square cavity flow in two dimensions is used as a benchmark test. Our results demonstrate that the ELBE does not improve the numerical stability of the SRT or the lattice Bhatnagar-Gross-Krook (LBGK) model. Our results also show that the MRT and TRT LB models are superior to the ELBE and LBGK models in terms of accuracy, stability, and computational efficiency and that the ELBE scheme is the most inferior among the LB models tested in this study, thus is unfit for carrying out numerical simulations in practice. Our study suggests that, to optimize the accuracy, stability, and efficiency in the MRT model, it requires at least three independently adjustable relaxation rates: one for the shear viscosity ν (or the Reynolds number Re), one for the bulk viscosity ζ, and one to satisfy the criterion imposed by the Dirichlet boundary conditions which are realized by the bounce-back-type boundary conditions.

DOI: 10.1103/PhysRevE.83.056710 PACS number(s): 47.11.−j, 47.15.−x, 47.45.Ab

I. INTRODUCTION

The lattice Boltzmann equation (LBE) has been used to solve a wide range of of problems in computational fluid dynamics (CFD) (cf. reviews [1,2] and references therein). There are several variations of the LBE, including the lattice Bhatnagar-Gross-Krook (LBGK) model or single-relaxation-time (SRT) model, the entropic model [3,4], and the two-relaxation-time (TRT) [5–7] and multiple-relaxation-time (MRT) [8–11] models. All these LB models can be derived from the linearized Boltzmann equation [12,13], and the difference between them resides in their collision terms. The LBGK model is the simplest in appearance and thus is also the most popular one. However, the LBGK model has several inherent deficiencies including numerical instability and inaccurate boundary locations [14,15]. The entropic LBE (ELBE) is intended to overcome the numerical instability of the LBGK model [3,4]. The MRT-LB model is the most general form derived from the linearized collision model within the theoretical framework of the LBE and kinetic theory—it includes all possible degrees of freedom to optimize the LBE, and it has been shown to be superior over the SRT models in terms of accuracy, stability, and computational efficiency [10,15,16]. The TRT model allows only two most important relaxation rates in the LBE; it retains some advantages of the MRT model in terms of accuracy and stability, while maintaining the simplicity of implementation and hence the computational efficiency.

While the aforementioned LB models have existed for quite some time, there has never been a comprehensive comparative evaluation to quantitatively assess the efficacy of these LB models for solving problems in CFD. In this work, we intend to compare the LBGK, ELBE, MRT, and TRT models in terms of their accuracy, stability, and computational efficiency for solving the incompressible Navier-Stokes equations in two dimensions (2D). We use the lid-driven square cavity flow in 2D as a benchmark test.

The remainder of the paper is organized as follows. Section II provides a succinct introduction of the LB models including the MRT, TRT, LBGK, and ELBE models; it also includes a brief discussion of the bounce-back (BB) boundary conditions (BCs). Section III presents the results of this study. We first briefly describe the benchmark test problem: the lid-driven square cavity flow in 2D. The LB results are compared with data obtained by using a pseudospectral method with multigrid and singularity subtraction technique [17,18]. We investigate the abilities of the LB schemes to compute the gross features of the flow, the flow fields near the boundary, the convergence behavior, the numerical stability, and computational efficiency. Our results expose the inherent deficiencies of the ELBE and LBGK schemes in terms of accuracy, stability, and efficiency. Finally, Sec. IV concludes the paper.

II. LATTICE BOLTZMANN EQUATION

A. Lattice Boltzmann models

The LBE is a discrete system that evolves on a d-dimensional lattice $\boldsymbol{x}_i \in \delta_x \mathbb{Z}^d$ and in discrete time $t_n \in \delta_t \mathbb{N}_0 := \delta_t\{0, 1, \ldots\}$. The LBE is derived from the kinetic theory and resembles the discrete velocity model of the Boltzmann equation in some aspects [19]. The discrete velocity set of the LBE, $\mathbb{V} := \{\boldsymbol{c}_i | i = 0, 1, \ldots, b\}$, usually is

---

[*] Corresponding author: lluo@odu.edu;http://www.lions.odu.edu/~lluo; FAX: +1 (757) 683-3885.

[†] wliao@odu.edu

[‡] ypeng@odu.edu

[§] zhangwei@stu.xjtu.edu.cn

symmetric, that is, $\mathbb{V} = -\mathbb{V}$, and has a zero velocity $\boldsymbol{c}_0 = \mathbf{0}$. The total number of discrete velocities in $\mathbb{V}$ is $q = (1 + b)$, including one zero velocity and b nonzero ones. An LB model with q velocities in d-dimensional space is usually denoted as a DdQq model. In this work, we use the D2Q9 model on a square lattice, of which the discrete velocity set $\{\boldsymbol{c}_i | i = 0, 1, \ldots, 8\}$ is

$$\boldsymbol{c}_i = \begin{cases} (0, 0), & i = 0, \\ (\pm 1, 0)c, (0, \pm 1)c, & i = 1\text{–}4, \\ (\pm 1, \pm 1)c, & i = 5\text{–}8, \end{cases} \tag{1}$$

where $c := \delta_x/\delta_t$.

In general, the LBE can be concisely written as the following:

$$\mathbf{f}(\boldsymbol{x}_i + \boldsymbol{c}\delta_t, t_n + \delta_t) - \mathbf{f}(\boldsymbol{x}_i, t_n) = \mathbf{\Omega}(\mathbf{f}), \tag{2}$$

where the bold-font symbols represent q-dimensional (column) vectors

$$\mathbf{f}(\boldsymbol{x}_i + \boldsymbol{c}\delta_t, t_n + \delta_t) =: [f_0(\boldsymbol{x}_i, t_n + \delta_t), \ldots, f_b(\boldsymbol{x}_i + \boldsymbol{c}_b\delta_t, t_n + \delta_t)]^\dagger,$$

$$\mathbf{f}(\boldsymbol{x}_i, t_n) =: [f_0(\boldsymbol{x}_i, t_n), f_1(\boldsymbol{x}_i, t_n), \ldots, f_b(\boldsymbol{x}_i, t_n)]^\dagger,$$
$$\mathbf{\Omega}(\mathbf{f}) = [\Omega_0(\boldsymbol{x}_i, t_n), \Omega_1(\boldsymbol{x}_i, t_n), \ldots, \Omega_b(\boldsymbol{x}_i, t_n)]^\dagger,$$

$\dagger$ denotes the transpose operation, $f_i(\boldsymbol{x}_j, t_n)$ is the distribution function corresponding to the discrete velocity $\boldsymbol{c}_i$, and Ω_i is the change in f_i due to collisions.

For the purpose of solving the incompressible Navier-Stokes equations, most collision models in the LBE (2) are based on the linearized collision operator. This study focuses on the following LB models: the MRT [8–11], the TRT [5–7], the SRT or the LBGK [20], and the entropic LB [3]. We first discuss the MRT model, of which the collision model can be written as

$$\mathbf{\Omega} = -\mathsf{M}^{-1} \cdot \hat{\mathsf{S}} \cdot [\mathbf{m} - \mathbf{m}^{(\text{eq})}], \tag{3}$$

where $\mathbf{m}$ and $\mathbf{m}^{(\text{eq})}$ represent the velocity moments of the distribution functions $\mathbf{f}$ and their equilibria, respectively,

$$\mathbf{m} = [m_0(\boldsymbol{x}_i, t_n), m_1(\boldsymbol{x}_i, t_n), \ldots, m_b(\boldsymbol{x}_i, t_n)]^\dagger,$$
$$\mathbf{m}^{(\text{eq})} = [m_0^{(\text{eq})}(\boldsymbol{x}_i, t_n), m_1^{(\text{eq})}(\boldsymbol{x}_i, t_n), \ldots, m_b^{(\text{eq})}(\boldsymbol{x}_i, t_n)]^\dagger,$$

M is a $q \times q$ matrix which linearly transforms the distribution functions $\mathbf{f} \in \mathbb{V} \equiv \mathbb{R}^q$ to the velocity moments $\mathbf{m} \in \mathbb{M} \equiv \mathbb{R}^q$,

$$\mathbf{m} = \mathsf{M} \cdot \mathbf{f}, \quad \mathbf{f} = \mathsf{M}^{-1} \cdot \mathbf{m}, \tag{4}$$

and $\hat{\mathsf{S}}$ is a non-negative $q \times q$ diagonal relaxation matrix [8–11].

The LB method was created as an alternative CFD solver—it is *not* intended as a solver for the Boltzmann equation. The quantities of interest to macroscopic hydrodynamics, such as the density ρ, the flow momentum $\rho\boldsymbol{u}$, and the total energy ρE, as well as their fluxes, are (velocity) moments of the single-particle mass distribution function $f(\boldsymbol{x}, \boldsymbol{\xi}, t)$ in the phase space $\Gamma := (\boldsymbol{x}, \boldsymbol{\xi})$, which satisfies the Boltzmann equation, and it is therefore natural to deal with equations of moments (cf., e.g., [21]). The MRT-LBE is formulated in the spirit and tradition of kinetic method in this regard: The collision process is approximated as linear relaxations in the space of moments, and the relaxation rates are directly related to transport coefficients, while the transport process is independently executed in velocity space. The MRT-LBE is not only theoretically elegant, but practically advantageous, as we demonstrate through this study.

Corresponding to the nine discrete velocities of the D2Q9 LB model, $\{\boldsymbol{c}_i | i = 0, 1, \ldots, 8\}$, there are nine velocity moments $\{m_i | i = 0, 1, \ldots, 8\}$. The labeling (or the ordering) of these moments is arbitrary and we will use the convention given by Lallemand and Luo [9], that is, $m_0 = \delta\rho$, $m_1 = e$, $m_2 = \varepsilon$, $m_3 = j_x$, $m_4 = q_x$, $m_5 = j_y$, $m_6 = q_y$, $m_7 = p_{xx}$, and $m_8 = p_{xy}$. The conserved moments in the system are the density $\rho = \rho_0 + \delta\rho$, where $\rho_0 = 1$ and $\delta\rho$ are the mean density and the density fluctuation, respectively, the flow momentum $\boldsymbol{j} = (j_x, j_y) = \rho_0\boldsymbol{u}$, where $\boldsymbol{u} = (u, v)$ is the flow velocity. (Because energy is *not* a conserved quantity in the LB models considered in the present, thus these LB models are *athermal*.) The physical significance of the other six nonconserved moments can be found in the literature [8–11]. The equilibria of the conserved moments are themselves, and the equilibria of the nonconserved moments are given below:

$$e^{(\text{eq})} = -2\delta\rho + \frac{3}{\rho_0}\left(j_x^2 + j_y^2\right), \tag{5a}$$

$$\varepsilon^{(\text{eq})} = \delta\rho - \frac{3}{\rho_0}\left(j_x^2 + j_y^2\right), \tag{5b}$$

$$\left(q_x^{(\text{eq})}, q_y^{(\text{eq})}\right) = -(j_x, j_y), \tag{5c}$$

$$p_{xx}^{(\text{eq})} = \frac{1}{\rho_0}\left(j_x^2 - j_y^2\right), \quad p_{xy}^{(\text{eq})} = \frac{1}{\rho_0} j_x j_y. \tag{5d}$$

By considering only $\delta\rho$ in various parts of the equilibria pertaining to the mass conservation, the effects of the round-off error can be reduced [22,23], especially when $|\delta\rho| \ll 1$. Since the density fluctuation $\delta\rho$ and the flow velocity $\boldsymbol{u}$ are decoupled, the above model approximates incompressible flows [22]. With ordering of the discrete velocities $\{\boldsymbol{c}_i\}$ and the moments $\{m_i\}$ given above, the transformation matrix M is [8–11]

$$\mathsf{M} = \begin{pmatrix} 1 & 1 & 1 & 1 & 1 & 1 & 1 & 1 & 1 \\ -4 & -1 & -1 & -1 & -1 & 2 & 2 & 2 & 2 \\ 4 & -2 & -2 & -2 & -2 & 1 & 1 & 1 & 1 \\ 0 & 1 & 0 & -1 & 0 & 1 & -1 & -1 & 1 \\ 0 & -2 & 0 & 2 & 0 & 1 & -1 & -1 & 1 \\ 0 & 0 & 1 & 0 & -1 & 1 & 1 & -1 & 1 \\ 0 & 0 & -2 & 0 & 2 & 1 & 1 & -1 & -1 \\ 0 & 1 & -1 & 1 & -1 & 0 & 0 & 0 & 0 \\ 0 & 0 & 0 & 0 & 0 & 1 & -1 & 1 & -1 \end{pmatrix}. \tag{6}$$

Note that rows 4 and 6 uniquely define the ordering (or labeling) of the discrete velocities $\{\boldsymbol{c}_i\}$. Correspondingly, the diagonal matrix of non-negative relaxation rates $0 < s_i < 2$ is given by

$$\mathsf{S} = \text{diag}(0, s_e, s_\varepsilon, 0, s_q, 0, s_q, s_\nu, s_\nu). \tag{7}$$

With the equilibria given by Eqs. (5), the first-order nonequilibrium parts of the nonconserved moments are

$$p_{xx}^{(1)} = -\frac{2}{3s_\nu}(\partial_x j_x - \partial_y j_y), \tag{8a}$$

$$p_{xy}^{(1)} = -\frac{1}{3s_\nu}(\partial_y j_x - \partial_x j_y), \tag{8b}$$

$$e^{(1)} = -\frac{2}{s_e}(\partial_x j_x + \partial_y j_y), \tag{8c}$$

$$\varepsilon^{(1)} = \frac{2}{s_\varepsilon}(\partial_x j_x + \partial_y j_y), \tag{8d}$$

$$q_{x,y}^{(1)} = 0. \tag{8e}$$

The speed of sound in a quiescent media for the D2Q9 model is

$$c_s = \frac{1}{\sqrt{3}}c, \tag{9}$$

and the shear viscosity ν and the bulk viscosity ζ are

$$\nu = \frac{1}{3}\left(\frac{1}{s_\nu} - \frac{1}{2}\right)c\delta_x, \tag{10a}$$

$$\zeta = \frac{1}{3}\left(\frac{1}{s_e} - \frac{1}{2}\right)c\delta_x, \tag{10b}$$

where s_ν is the relaxation rate for the moments p_{xx} and p_{xy}, which are related to the off-diagonal elements of the stress tensor, and s_e is the relaxation rate for the moment e, which is related to the diagonal elements of the stress tensor. The dissipation for (longitudinal) sound waves or density fluctuations in the system is $(\nu + \zeta)/2$.

If we set the relaxation rates for the even-order nonconserved moments (i.e., e, ε, p_{xx}, and p_{xy}) to $s_+ = 1/\tau$ and those for the odd-order ones (i.e., q_x and q_y) to [14,24,25]

$$s_q = 8\frac{(2 - s_\nu)}{(8 - s_\nu)} = 8\frac{(2\tau - 1)}{(8\tau - 1)} = \frac{16\nu}{8\nu + 1}, \tag{11}$$

then the MRT model becomes the TRT model [5–7]. If we set all relaxation rates $\{s_i\}$ equal to $1/\tau$, then the MRT model reduces to the LBGK model with SRT, of which the equilibrium distribution functions are

$$f_i^{(\text{eq})} = w_i\left[\delta\rho + \rho_0\left\{\frac{\boldsymbol{c}_i\cdot\boldsymbol{u}}{c_s^2} + \frac{1}{2}\left(\frac{(\boldsymbol{c}_i\cdot\boldsymbol{u})^2}{c_s^4} - \frac{\boldsymbol{u}\cdot\boldsymbol{u}}{c_s^2}\right)\right\}\right], \tag{12}$$

where $w_0 = 4/9$ for $\|\boldsymbol{c}_0\| = 0$, $w_{1,2,3,4} = 1/9$ for $\|\boldsymbol{c}_{1,2,3,4}\| = c$, $w_{5,6,7,8} = 1/36$ for $\|\boldsymbol{c}_{5,6,7,8}\| = \sqrt{2}c$, and $c_s = c/\sqrt{3}$. The collision model in the LBGK equation is

$$\Omega_i = -\frac{1}{\tau}\left[f_i - f_i^{(\text{eq})}\right]. \tag{13}$$

The ELBE proposed by Ansumali *et al.* [3] has the BGK collision term with the following equilibria:

$$f_i^{(\text{eq})} = w_i\rho\prod_{\alpha=1}^{2}(2 - S_\alpha)\left(\frac{2u_\alpha + cS_\alpha}{c - u_\alpha}\right)^{c_{i\alpha}/c}, \tag{14a}$$

$$S_\alpha := \sqrt{1 + \left(\frac{u_\alpha}{c_s}\right)^2}, \tag{14b}$$

where Greek subscript α denotes the Cartesian coordinates $\{x, y\}$ or $\{1, 2\}$ in 2D and $c_{i\alpha}/c \in \{-1, 0, +1\}$. The above equilibria can also be rewritten as [26]

$$f_i^{(\text{eq})} = \rho\left(-\frac{1}{2}\right)^{\frac{|c_{ix}|+|c_{iy}|}{c}}\left[\frac{c_s^2}{c^2}(2S_x - 1) + \left(-\frac{u_x c_{ix}}{c^2}\right)^{\frac{|c_{ix}|}{c}}\right] \times\left[\frac{c_s^2}{c^2}(2S_y - 1) + \left(-\frac{u_y c_{iy}}{c^2}\right)^{\frac{|c_{iy}|}{c}}\right]. \tag{15}$$

For both the LBGK and ELBE models with one relaxation time τ given above, the shear viscosity ν and the bulk viscosity ζ are given by [9]

$$\nu = \frac{1}{3}\left(\tau - \frac{1}{2}\right)c\delta_x, \quad \zeta = \nu. \tag{16}$$

The attenuation coefficient (or dissipation) for acoustic waves (or the density fluctuation) in the system is $\zeta + \nu/2 = \nu$ for the LBGK models. Consequently, the LBGK models are prone to numerical instabilities when ν is small (or τ close to 1/2), because there is no ν-independent mechanism to keep the density fluctuation in check.

A few remarks regarding the ELBE model [3] described above are in order here. First of all, the equilibrium moments computed from the equilibrium distributions of Eqs. (14) or (15) with $c_s^2 = c^2/3$ are

$$e^{(\text{eq})} = 2\rho(S_x + S_y - 3), \tag{17a}$$

$$\varepsilon^{(\text{eq})} = \rho(2S_x - 3)(2S_y - 3), \tag{17b}$$

$$q_{x,y}^{(\text{eq})} = \rho(2S_{y,x} - 3)\frac{u_{x,y}}{c}, \tag{17c}$$

$$p_{xx}^{(\text{eq})} = \frac{2}{3}\rho\,(S_x - S_y), \tag{17d}$$

$$p_{xy}^{(\text{eq})} = \rho u_x u_y. \tag{17e}$$

Thus, except $p_{xy}^{(\text{eq})}$ and the terms involving $\delta\rho\cdot\boldsymbol{u}$, which are neglected by the incompressibility approximation [22], one difference between the ELBE and MRT-LBE is the $O(u^3)$ terms in the odd-order equilibrium moments, $q_x^{(\text{eq})}$ and $q_y^{(\text{eq})}$, which affect the Galilean invariance of the model [9], while the difference in the even-order equilibrium moments, $e^{(\text{eq})}$, $\varepsilon^{(\text{eq})}$, and $p_{xx}^{(\text{eq})}$, is of the terms of the order $O(u^4)$.

Second, based on our experience and understanding of the LBE, it is unclear theoretically how the ELBE with a *constant* relaxation parameter τ can improve the numerical stability of the LBGK scheme, as it has been advocated [3,4]. Furthermore, if the equilibria of Eqs. (14a) are replaced by their low-order Taylor expansions in $\boldsymbol{u}$, as suggested in [26], then it can be shown *rigorously* that the equilibria of polynomial form cannot admit an H theorem [27,28] and the ELBE is no longer entropic. In this study we numerically demonstrate that the ELBE model does not improve the numerical stability of the LBGK model in any way, contrary to previous claims [3,4].

We would also like to comment on the general characteristics of the LBE. First of all, the relevant physical quantities of the LBE are the conserved quantities; that is, the density ρ and the momentum $\rho\boldsymbol{u}$ for the athermal LB models. The pressure p and the velocity $\boldsymbol{u}$ are derived or indirect quantities. The conserved quantities, ρ and $\rho\boldsymbol{u}$, obtained with the LBE can only approximate p and $\boldsymbol{u}$, which are the solutions of the incompressible Navier-Stokes equations [29]. Since the density ρ is an intrinsic variable of the LBE, the compressibility associated with the density fluctuation is inherent in the LBE. Thus, the second point is that *all* LB schemes are intrinsically compressible in the sense that the density is an essential variable and the velocity field is never divergence free. The so-called "incompressible" LB schemes (e.g., [22]) can only alter the compressibility effect *quantitatively*, but can never eliminate it entirely. Theoretically, the incompressible Navier-Stokes equations can be derived directly from the Boltzmann equation in the diffusive scaling limit $\delta_x^2/\delta_t = 1$ (cf. [29,30] and references therein), and the exponential tail of the Maxwellian equilibrium when $\|\boldsymbol{\xi}\| \to \infty$ is indispensable in this derivation. With a set of finite discrete velocities $\{\boldsymbol{c}_i | i = 0, 1, \ldots, b\}$, the LBE cannot possibly satisfy the Poisson equation exactly, which requires the pressure to propagate throughout the system instantaneously, that is, with a propagating speed of infinity. Thus, the LBE is intrinsically compressible and can only approximate the incompressible Navier-Stokes equations. The pressure p in the LBE is coupled to the density ρ through a simple equation of state $p = c_s^2\rho$ for ideal gases, and in this way the LBE is related to the artificial compressibility method [31,32].

It is also worth noting that the only important distinction between the so-called "incompressible" and the "compressible" LB schemes lies in the acoustics of the system. The speed of the sound waves in the incompressible LB schemes is incorrect (cf. Eq. (48) and relevant discussions in [9]),

$$\begin{aligned} C_s &= V\cos\phi \pm \sqrt{c_s^2 + V^2\cos^2\phi} \\ &= V\cos\phi \pm c_s\sqrt{1 + \mathrm{Ma}^2\cos^2\phi}, \end{aligned}$$

where $\mathrm{Ma} = V/c_s$, $V = \|\boldsymbol{V}\|$, $\boldsymbol{V}$ is the constant streaming velocity of the media, and ϕ is the angle between $\boldsymbol{V}$ and the wave vector $\boldsymbol{k}$ of the acoustic waves [9]. In order to have a correct speed of acoustic waves, $C_s = V\cos\phi \pm c_s$, one must use the compressible LB schemes, that is, replacing ρ_0 by ρ in the equilibria of Eqs. (5) and (12). Since we are only concerned with steady-state calculations in this study, while the incompressible approximation can improve computational efficiency a little by avoiding the divisions by ρ in computing the equilibria and possibly reduce the compressibility effect [22], its defect in the acoustic propagation will not affect the results negatively.

B. The bounce-back boundary conditions

The BB BCs in the LBE are used to realize the Dirichlet BCs. The BB BCs are easily to implement: When colliding with an impenetrable wall with a velocity $\boldsymbol{u}_{\mathrm{w}}$, the particle simply reverses its momentum normal to the wall and gains an additional momentum due to the wall velocity $\boldsymbol{u}_{\mathrm{w}}$, that is,

$$f_{\bar{\imath}}(\boldsymbol{x}_{\mathrm{b}}, t + \delta_t) = f_i(\boldsymbol{x}_{\mathrm{b}}, t) - 2\rho_0 w_i \frac{\boldsymbol{c}_i \cdot \boldsymbol{u}_{\mathrm{w}}}{c_s^2}, \tag{18}$$

where $f_{\bar{\imath}}$ and f_i correspond to the discrete velocity $\boldsymbol{c}_{\bar{\imath}}$ and $\boldsymbol{c}_i$, respectively, and $f_i(\boldsymbol{x}_{\mathrm{b}}, t)$ in the right-hand side of Eq. (18) is the postcollision distribution function; $\boldsymbol{c}_{\bar{\imath}} = -\boldsymbol{c}_i$; the component of $\boldsymbol{c}_i$ normal to the wall is pointing outward from fluid domain to the wall; $\boldsymbol{x}_{\mathrm{b}}$ is a fluid node adjacent to a wall boundary; and $\boldsymbol{u}_{\mathrm{w}}$ is the wall velocity at the point where the particle of the velocity $\boldsymbol{c}_i$ collides with the wall.

The BB BCs are implemented as follows. Beyond the boundary, an extra (ghost) layer of nodes is used to store the distribution functions f_i, which move out of the flow domain in the advection step.The collisions between these particles and the wall are accomplished by reversing themselves to $f_{\bar{\imath}}$ and gaining the amount of momentum $-2\rho_0 w_i \boldsymbol{c}_i \cdot \boldsymbol{u}_{\mathrm{w}}/c_s^2$; they are then copied to the fluids nodes where they came from through the advection.

The BB BCs have been studied in detail and are well understood [14,24,25]. The analytic solutions for the LBE with the BB BCs can be obtained for simple flows, such as the Poiseuille and Couette flows [24,25,33,34]. For the Poiseuille flow driven by a constant body force $G = \|\boldsymbol{\nabla} p\|$ and with its walls parallel to lattice lines, the actual channel width H observed in the simulations is given by [14,24,25]

$$H^2 = H_{1/2}^2 + 4\Delta^2 - 1, \tag{19a}$$

$$\Delta = \frac{4}{3}\left(\frac{1}{s_\nu} - \frac{1}{2}\right)\left(\frac{1}{s_q} - \frac{1}{2}\right), \tag{19b}$$

where $H_{1/2} := N\delta_x$ and N is the number of fluid nodes across the channel. That is, only when the relationship between s_q and s_ν of Eq. (11) is satisfied, $\Delta = 1/2$ and $H = H_{1/2}$; the no-slip BCs at the channel walls are indeed satisfied at the $\delta_x/2$ beyond the last fluid nodes; and the maximum velocity at the channel center line is $U_{\max} = GH^2/8\nu$. If $H \neq H_{1/2}$, then the LB solution is *inconsistent* with the incompressible Navier-Stokes solution we desire.

For the ELBE and the LBGK schemes with only one relaxation parameter τ, Eq. (19b) becomes

$$\Delta = \frac{4}{3}\left(\tau - \frac{1}{2}\right)^2 = 12\nu^2.$$

Therefore, $\Delta = 1/2$ if and only if $\nu = 1/(2\sqrt{6})$ (or $\tau = 1/2 + \sqrt{6}/4 \approx 1.1123$). In the interval $1/2 < \tau \leqslant 1/2 + \sqrt{6}/4$, we have $-1 < (4\Delta^2 - 1) \leqslant 0$ or $0 < \Delta \leqslant 1/2$. Consequently, the error of the inaccurate boundary location is within one lattice spacing δ_x. This explains why the LBGK simulations of flows of high Reynolds number with $\tau < 1$ have relatively small errors at the boundary. Since this error at the boundary is quadratic in ν (or τ), it becomes considerable or even intolerable when $\tau \gg 1$, which is the case for the Stokes or creeping flows and is practiced in simulations of flow through porous media [14,15]. This error of the LBGK schemes with the BB-type BCs is ostentatiously manifested in simulations of flow through porous media with very low Reynolds numbers—the permeability obtained by the LBGK schemes is viscosity dependent, which is unphysical [14,15].

Due to the intuitive nature of the BB BCs, it is often mistakenly *assumed* that, in the ELBE and LBGK schemes, the imposed Dirichlet BCs are indeed satisfied either right on the last fluid nodes adjacent to boundary or one half or one full grid spacing beyond them. This forms the basis of the misguided idea that the nonzero velocity in the vicinity of the last fluid nodes can mimic the Knudsen layer in rarefied flows (e.g., [35–37]). However, a close examination shows that the ELBE or LBGK schemes with the BB-type BCs are inadequate to model the Knudsen layer for the following reasons. The first is that, theoretically, the LBE is a truncated model valid for the Navier-Stokes equations and is incapable of modeling higher-order moments of the distribution function [38–41]. The second is that the velocity near the boundary depends on the grid resolution N; thus, the solution with fixed Re, Ma, and Kn does not converge as N increases [41]. A more detailed discussion of this point is deferred to Sec. III C.

III. RESULTS AND DISCUSSIONS

A. Lid-driven square cavity flow in two dimensions

We use the lid-driven square cavity flow in 2D as a test case to compare the lattice Boltzmann models. The 2D lid-driven flow prescribed by the 2D incompressible Navier-Stokes equation on a square domain $\Omega := (x, y) \in [0, L] \times [0, L] = [0, 1] \times [0, 1]$ is

$$\begin{gathered}\partial_t \boldsymbol{u} + \boldsymbol{u}\cdot\nabla\boldsymbol{u} = -\nabla p + \nu\nabla^2\boldsymbol{u}, \quad \nabla\cdot\boldsymbol{u} = 0\,, \\ \boldsymbol{u}(x, 1) = (U, 0),\ \boldsymbol{u}(x, 0) = \boldsymbol{u}(0, y) = \boldsymbol{u}(1, y) = \boldsymbol{0}\,,\end{gathered} \tag{20}$$

where $\boldsymbol{u}(\boldsymbol{x}, t)$ and $p(\boldsymbol{x}, t)$ are the velocity and the pressure field, respectively, and U is the sliding velocity of the top wall. The Reynolds number of the flow is defined by the sliding velocity U, the dimension L of the cavity, and the viscosity ν, that is, $\mathrm{Re} = UL/\nu$.

The 2D lid-driven square cavity flow has been studied extensively and employed by many as a benchmark test (cf., e.g., [17,18,42–45]). While the geometry of the flow domain is simple, the flow exhibits complicated features. Small vortices developed at the corners and other locations can be difficult to capture numerically for they are weak and small. The flow becomes unsteady when the Reynolds number is beyond a certain critical value and eventually becomes turbulent. In this work we will restrict ourselves to the steady states of the flow with Re = 100, 400, and 1000. The criterion for reaching steady state in the LB simulations is given by

$$\frac{\sum_i \|\boldsymbol{u}(\boldsymbol{x}_i, t_n + 1000\delta_t) - \boldsymbol{u}(\boldsymbol{x}_i, t_n)\|_2}{\sum_i \|\boldsymbol{u}(\boldsymbol{x}_i, t_n)\|_2} < 10^{-12}, \tag{21}$$

where $\|\boldsymbol{u}\|_2$ denotes the L^2 norm of $\boldsymbol{u}$. We compare the LB simulations with the results obtained by using an explicit Chebyshev pseudospectral (PS) multigrid (MG) method (cf. [18] and references therein) together with a singularity subtraction technique (cf. [17] and references therein) to deal with the corner singularities. With the singularity subtraction technique, PS-MG methods can yield very accurate results effectively and efficiently [17,18].

For the LB simulations, the viscosity in the units of δ_x and δ_t is determined by

$$\nu = \frac{UL}{\mathrm{Re}}, \tag{22}$$

where $U = 0.1c$ unless otherwise stated and $L = N_x\delta_x$. Therefore,

$$\tau = \frac{1}{s_\nu} = 3\nu + \frac{1}{2} = \frac{3UN\delta_x}{\mathrm{Re}} + \frac{1}{2}. \tag{23}$$

For the MRT and TRT models, Eq. (11) is used to determine the value of s_q, which is the relaxation rate for the heat fluxes q_x and q_y. The other two relaxation rates, s_e for the energy mode and s_ε for the energy square mode, are set to 1.64 and 1.54, respectively [9]. We use the BB BCs in the LB simulations. The nodes on the top two corners belong to the moving lid in the LB simulations.

The value of $U = 0.1c$ is not chosen entirely arbitrarily—it is a compromise between accuracy and computational efficiency. The value of U cannot be too large or the LB code becomes unstable. Also the compressibility error in the LBE is of $O(U^2)$ [29,43]; therefore, U should be as small as possible for the sake of accuracy. As a practical rule, one should restrict $\|\boldsymbol{u}(\boldsymbol{x}, t)\| < 0.2$ throughout the entire flow domain and for all time so that flow is nominally incompressible. On the other hand, larger U also means better computational efficiency, because the number of iterations to reach steady state, N_t, is proportional to the hydrodynamic diffusive time scale in the system, that is, $N_t \propto N^2/\nu = \mathrm{Re}N/U = c_s\mathrm{Re}N/\mathrm{Ma}$. Thus, the number of iterations N_t and the computational time are inversely proportional to U with both the mesh resolution N and the Reynolds number Re fixed. One can also see that increasing U effectively increases the Courant-Friedrichs-Lewy (CFL) number, thus decreases the computational time as a consequence.[1]

In PS methods, both the stream function ψ and the vorticity ω can be obtained analytically from the velocity $\boldsymbol{u}$. In the LBE, ψ is computed by using Simpson's rule for numerical integration:

$$\begin{aligned}\psi(x_{i+1}, y_j) = \psi(x_{i-1}, y_j) - \frac{\delta_x}{6}[&v(x_{i-1}, y_j) \\ &+ 4v(x_i, y_j) + v(x_{i+1}, y_j)],\end{aligned} \tag{24}$$

where $\psi(x = 0, y) = 0$, and the vorticity ω are computed from $\boldsymbol{u}$ by using the following finite difference formulas:

$$\begin{aligned}\partial_x u(x_i, y_j) \approx\ & u(x_{i+1}, y_j) - u(x_{i-1}, y_j) \\ & - \frac{1}{4}[u(x_{i+1}, y_{j+1}) - u(x_{i-1}, y_{j+1}) \\ & - u(x_{i-1}, y_{j-1}) + u(x_{i+1}, y_{j-1})],\end{aligned} \tag{25a}$$

$$\begin{aligned}\partial_y u(x_i, y_j) \approx\ & u(x_i, y_{j+1}) - u(x_i, y_{j-1}) \\ & - \frac{1}{4}[u(x_{i+1}, y_{j+1}) + u(x_{i-1}, y_{j+1}) \\ & - u(x_{i-1}, y_{j-1}) - u(x_{i+1}, y_{j-1})].\end{aligned} \tag{25b}$$

Note that the above formulas used to compute ψ and ω are valid only in the interior of the flow domain $\{(x_i, y_j)|2 \leqslant i \leqslant (N_x - 1), 2 \leqslant j \leqslant (N_y - 1)\}$. For the fluid nodes next to the

---

[1] The CFL condition requires that $U < \Delta x/\Delta t$, where U is the characteristic velocity of the flow, and Δx and Δt are the grid spacing and the time step size, respectively, both of which are free parameters to be chosen. For the LBE, the incompressibility condition requires that $U/c_s < \mathrm{Ma}_*$, where $\mathrm{Ma}_* \approx 0.3$ is the approximate upper bound of the Mach number, that is, $U < (\mathrm{Ma}_*/\sqrt{3})\delta_x/\delta_t$. Therefore, the Mach number limit in the LBE can be seen in the way similar to the CFL condition. However, it is important to stress that the CFL condition and the Mach number limit are *not* equivalent.

boundary or on the boundary nodes, special consideration must be given because the distance between the last fluid nodes and the boundary is only $\delta_x/2$ as opposed to δ_x (cf. the discussion in Sec. II B). For the fluid nodes next to the left boundary $x = 0$, that is, $\forall (x_1, y_j)\ 1 \leqslant j = N$, the following formula is used:

$$\partial_x u(x_1, y_j) \approx \frac{1}{3}[u(x_2, y_j) + 3u(x_1, y_j) - 4u(x_0, y_j)], \tag{26}$$

where (x_0, y_j) denotes a node on the left wall $x = 0$. Note that the velocity $\boldsymbol{u}$ is specified by the BCs at the boundaries; thus, the above formula can be simplified to

$$\partial_x u(x_1, y_j) \approx \frac{1}{3}[u(x_2, y_j) + 3u(x_1, y_j)],$$

because $\boldsymbol{u}(x = 0, y) = 0$. Similar formulas can be devised for the right, top, and bottom boundaries. On the boundary, we use Tom's formula to compute the vorticity:

$$\omega(x_0, y_j) = 2v(x_1, y_j), \tag{27a}$$

$$\omega(x_i, y_0) = 2u(x_i, y_1), \tag{27b}$$

$$\omega(x_{N+1}, y_j) = -2v(x_N, y_j). \tag{27c}$$

$$\omega(x_i, y_{N+1}) = 2[U - u(x_i, y_N)]. \tag{27d}$$

At the four corners, we simply compute the vorticity as the following:

$$\omega(x_0, y_0) = \omega(x_{N+1}, y_0) = 0, \tag{28a}$$

$$\omega(x_0, y_{N+1}) = \omega(x_{N+1}, y_{N+1}) = 2U. \tag{28b}$$

B. General flow features

We first compare the pressure $p(x, y)$, the stream function $\psi(x, y)$, and vorticity $\omega(x, y)$ obtained by the PS and LB methods. We found that, in many cases, the results obtained by the MRT-LB and TRT-LB schemes are very close to each other; so are those obtained by the LBGK and ELBE schemes. Therefore, we only show the MRT-LB and ELBE results unless otherwise stated. For the PS method [18], the number of collocation points in each dimension is $N = 96$, and the mesh size for the LB simulations presented in this section is $N_x \times N_y = 129^2$ unless otherwise stated. In LB simulations, we always use an odd number of grid points in each dimension to reduce the oscillations due to the spurious conserved quantities [46,47].

In Fig. 1, we show p, ψ, and ω with Re = 100 ($\tau = 0.887$ and $1/s_q \approx 0.984\,496\,125$) obtained by the PS method and the MRT-LB and ELBE schemes. The fields of p, ψ, and ω are normalized by U^2, UL, and U/L, respectively, where U is the sliding velocity of the top boundary and $L = N_x\delta_x = N_x$ is the dimension of the cavity in the lattice units of $\delta_x = \delta_t = 1$. The flow fields obtained by the MRT-LB and ELBE schemes are very close to the PS-MG results in terms of vorticity locations and general features of p, ψ, and ω.

When the Reynolds number Re is increased to Re = 400 ($\tau = 0.596\,75$ and $1/s_q \approx 2.437\,984\,495$), as shown in Fig. 2, the pressure field p and the vorticity field ω obtained by using the ELBE scheme start to oscillate in the upper-left corner, while those obtained by the MRT-LB and TRT-LB schemes remain close to the PS results without oscillations. The oscillations in the ELBE simulations are, in part, due to the fact that there is insufficient dissipation to the higher-order moments in the model. This is evident because the results obtained by using the TRT-LB scheme do not exhibit any oscillation; that is, a larger dissipation to the heat flux modes (q_x, q_y) is sufficient to prevent the oscillation.

When the Reynolds number Re is further increased to Re = 1000 ($\tau = 0.5387$ and $1/s_q \approx 5.344\,961\,24$), as shown in Fig. 3, the oscillations in both the pressure field p and the vorticity field ω obtained by using the ELBE scheme become quite severe, for lack of sufficient dissipation to the higher-order moments, while the results obtained by both the MRT-LB and the TRT-LB schemes remain free of oscillations and close to the PS solutions.

We observe that the general features in the vorticity fields obtained by both the TRT-LB and the MRT-LB schemes agree with the PS results better than the pressure field p does. This is expected because the pressure field p in the LBE is not solved as accurately as the velocity field $\boldsymbol{u}$ [29]. To make a closer examination of the oscillations in p and ω observed in the ELBE and LBGK schemes, we also carry out simulations at Re = 1000 with a larger mesh size of $N^2 = 257^2$ ($\tau = 0.5771$). In Fig. 4 we show the pressure field p and the vorticity field ω in the small area at the upper left corner $(x, y) \in [0, 0.1] \times [0.9, 1.0]$ where the ELBE and LBGK simulations oscillate severely. Because the results of the ELBE and LBGK schemes are so similar to each other, only the results obtained by using the ELBE scheme are shown in Fig. 4. We found that the ELBE scheme does not reduce the oscillations in the simulation; consequently, it does not improve the numerical stability of the LBGK scheme, which are discussed further later. The results obtained by the TRT-LB and MRT-LB schemes are very close to each other and much closer to the PS results (which are not shown in the figure, but are discussed later). We note that the LB schemes are only first-order accurate for the pressure field p [29]. Thus, the pressure field obtained by using the LB schemes is expected to be significantly different from the PS solution. We also note that the vorticity field obtained by using the ELBE and LBGK schemes is less oscillatory than the pressure fields.

We compile in Tables I and II, respectively, the positions of the primary and two secondary vortices, as well as the intensities of the pressure p, the stream function ψ, and the vorticity ω at the vortex centers, which are determined by the locations of local extrema of the stream function ψ. In these tables, we also include the data obtained by using the PS methods [17,18]. For the data obtained by a PS method [18], the flow fields are interpolated to a very fine, equispaced mesh with the grid spacing of $10^{-6}L$, and the vortex centers and their intensities are found on the fine mesh. In the Tables I and II, blank entries indicate the results obtained by using the LB methods which have at least six significant digits identical to that obtained by using the MRT-LBE with the same mesh size. For example, in Table I, in the case of Re = 100 with $N = 513$, the results obtained by using the TRT-LBE agree with that obtained by the MRT-LBE in at least six significant digits; thus, the entries corresponding to the TRT-LB results are left blank in the table. Note that for the LB results, the vortex centers are determined by finding extrema of the stream function ψ on grid points; thus, the error in the vortex centers is of the order $O(1/N)$.

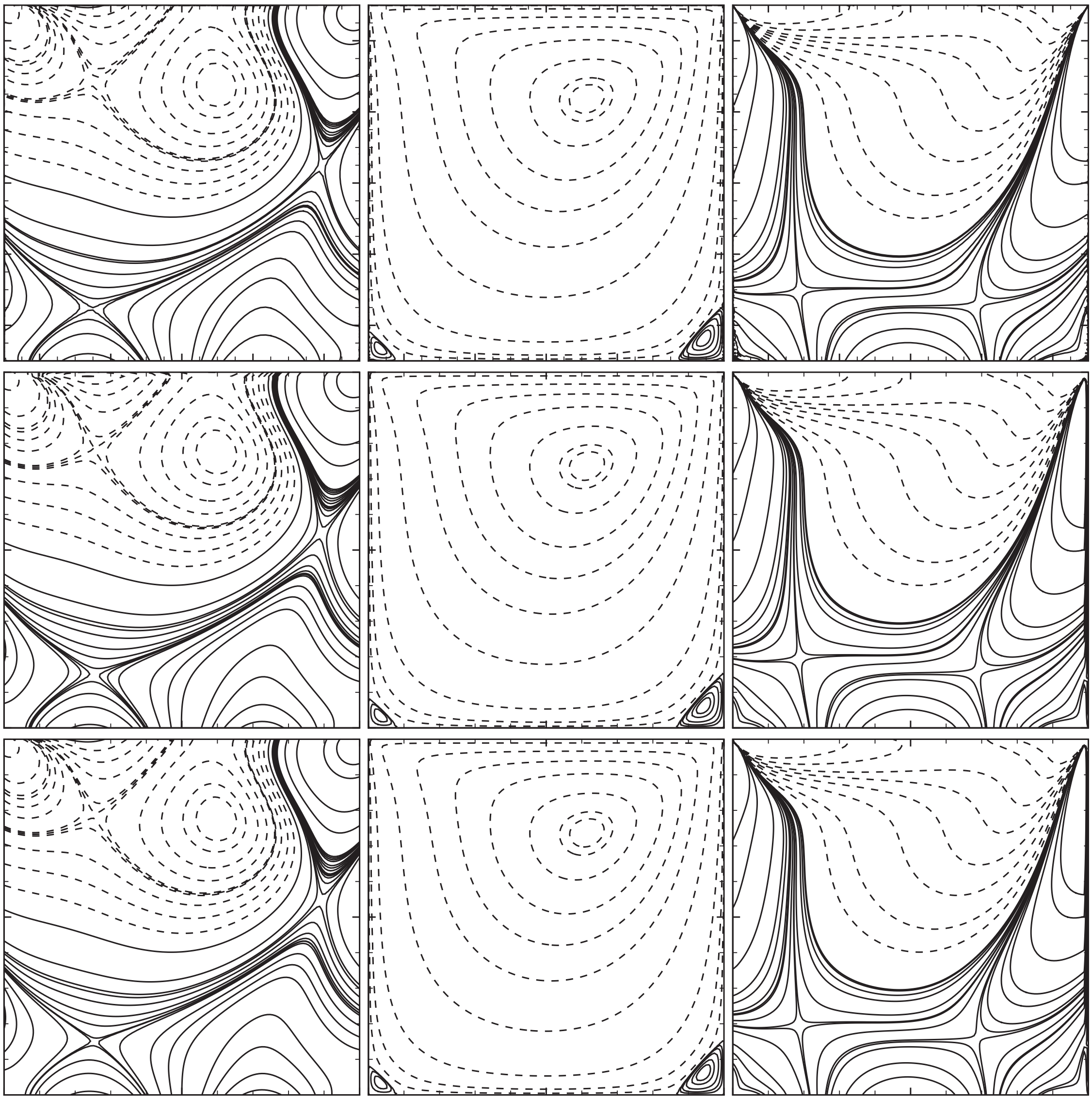

FIG. 1. Re = 100. From left to right: contours of pressure p, stream function ψ, and vorticity ω. From top: the PS-MG method ($N = 96$) and the MRT-LB and ELBE schemes ($N_x \times N_y = 129^2$). Solid and dashed lines denote contours of positive and negative values, respectively.

Clearly, the positions of the primary and secondary vortex centers obtained by the LB schemes are identical in most cases, and the difference is only one grid spacing $\delta_x = 1/N$ at most. The LB results for the vortex positions also agree with those obtained by using PS-MG methods [17,18]. The intensities of p, ψ, and ω at the vortex centers obtained by using different methods agree well with each other for the given mesh resolution. For the primary vortex, the intensities of both the stream function ψ and the vorticity ω at the vortex center have agreement of three significant digits, while the pressure p obtained by using the LB schemes only achieves one or two digits agreement with the PS-MG data, and the discrepancy in p clearly grows as Re increases. The errors in the LB results are consistent with the density fluctuation in the system, which is a measure of the compressibility effect in the system. The values of ω, ψ, and p at the primary vortex center are of the order $O(1)$, $O(10^{-1})$, and $O(10^{-2})$, respectively. With $U = 0.1c$ and $\mathrm{Ma} = 0.1/\sqrt{3} \approx 0.1732$, the compressibility effect is of the order $O(\mathrm{Ma}^2) = O(10^{-3})$, which is not negligible when compared with the intensity of p at the vortex centers. A more quantitative discussion of the compressibility effect will be deferred to Sec. III D.

The sizes of the secondary vortices are much smaller than that of the primary one, and the intensities of p, ψ, and ω at the secondary vortex centers are significantly weaker than those at the primary vortex center, especially at low Reynolds numbers. For example, with Re = 100, at the center of the secondary vortex at the lower-right corner, the intensities of p, ψ, and ω are weaker than their counterparts at the primary vortex center by a factor about 4, 10^4, and 10^2, respectively, and the vortex at the lower-left corner is even smaller and weaker. Nevertheless, the LB simulations are able to quantitatively capture the general flow features.

With Re = 1000, a tertiary vortex appears at the lower-right corner, which can be accurately captured by the PS method with at least five significant digits

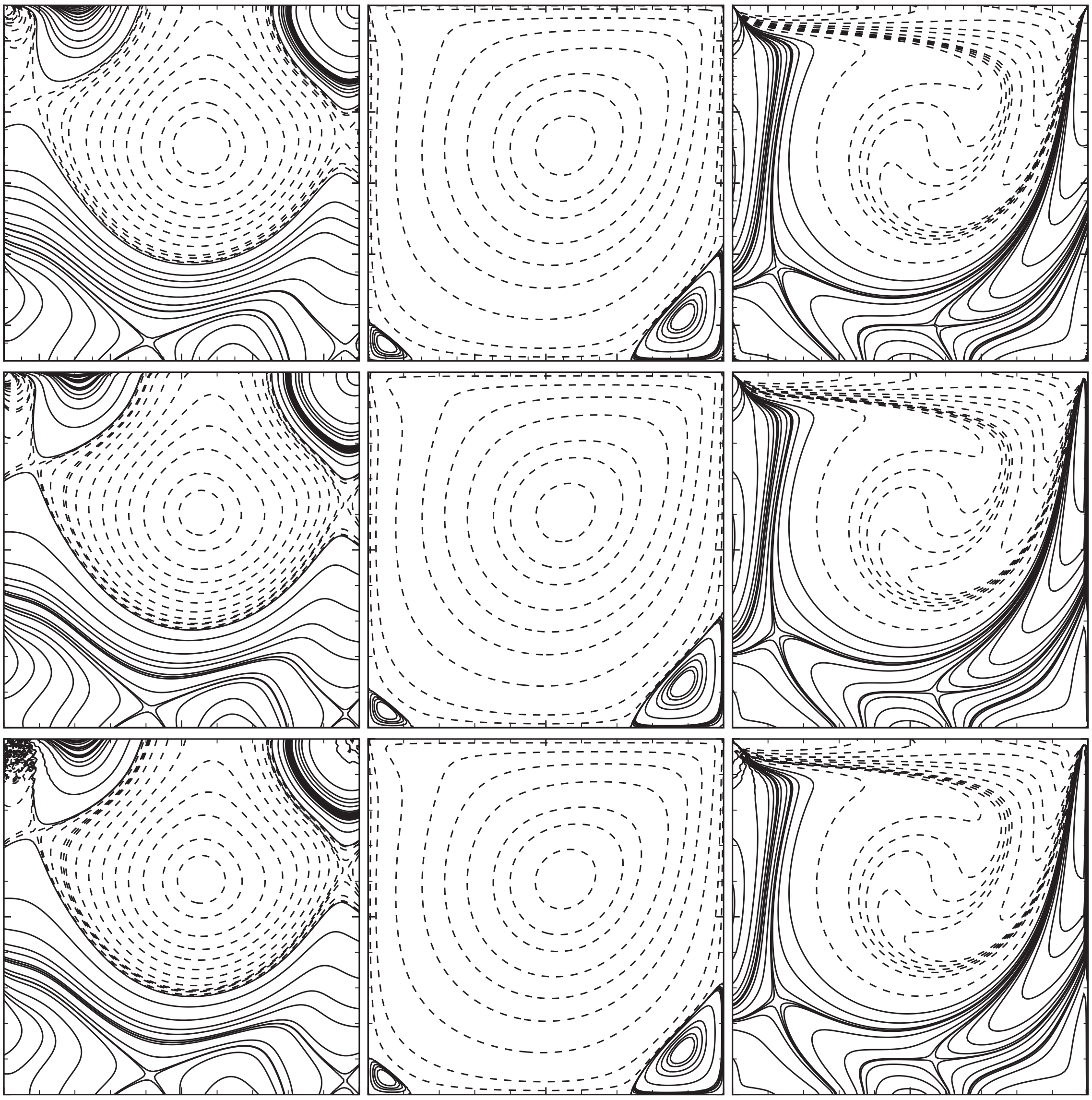

FIG. 2. Re = 400. Similar to Fig. 1.

(cf. Table 14 in [17]). Both the MRT-LB and the TRT-LB schemes can capture the tertiary vortex with a resolution of $N = 129$, but not the ELBE and LBGK schemes. However, with a higher resolution of $N = 257$, all the LB schemes can capture the tertiary vortex, as shown in Fig. 5. We note that the stream function ψ obtained by using the PS-MG method [18] exhibits high-frequency oscillations near the right wall, which affects the results of the tertiary vortex. We tabulate the results for the tertiary vortex in Table III. The values of p, ψ, and ω of the PS-MG method [18] given in Table III are estimated by using data probing tool of Tecplot, which is used to generate the contour plots of Fig. 5. We note that the stream function ψ at the tertiary vortex center is extremely weak—it is of the order $O(10^{-8})$. With the resolution of $N^2 = 257^2$, the intensities of ψ at the tertiary vortex center obtained by both the MRT-LB and the TRT-LB schemes are about 20% weaker than the very accurate value obtained by using a PS-MG method [17], while the result of the ELBE scheme is weaker than the PS-MG result by a factor of about 5. It is remarkable that the LB schemes can capture the tertiary vortex at all, in spite of its minuscule extent and weak intensities.

C. Flow fields near the boundary

In the previous section, we show that all LB schemes can capture general flow features of the flow, such as locations and intensities of primary and secondary vortices. We observe that the pressure fields near the top sliding lid obtained with the TRT-LB and MRT-LB schemes differ from each other, indicating the effects of the relaxation rates s_e and s_ε on the pressure field p. This is conceivable because s_e directly affects the dissipation of the acoustics (pressure waves) in the system, while s_ε affects it indirectly through a higher-order moment ε.

There are only two adjustable relaxation rates in the MRT-LB scheme: s_e and s_ε; the other two relaxation rates, s_ν and s_q,

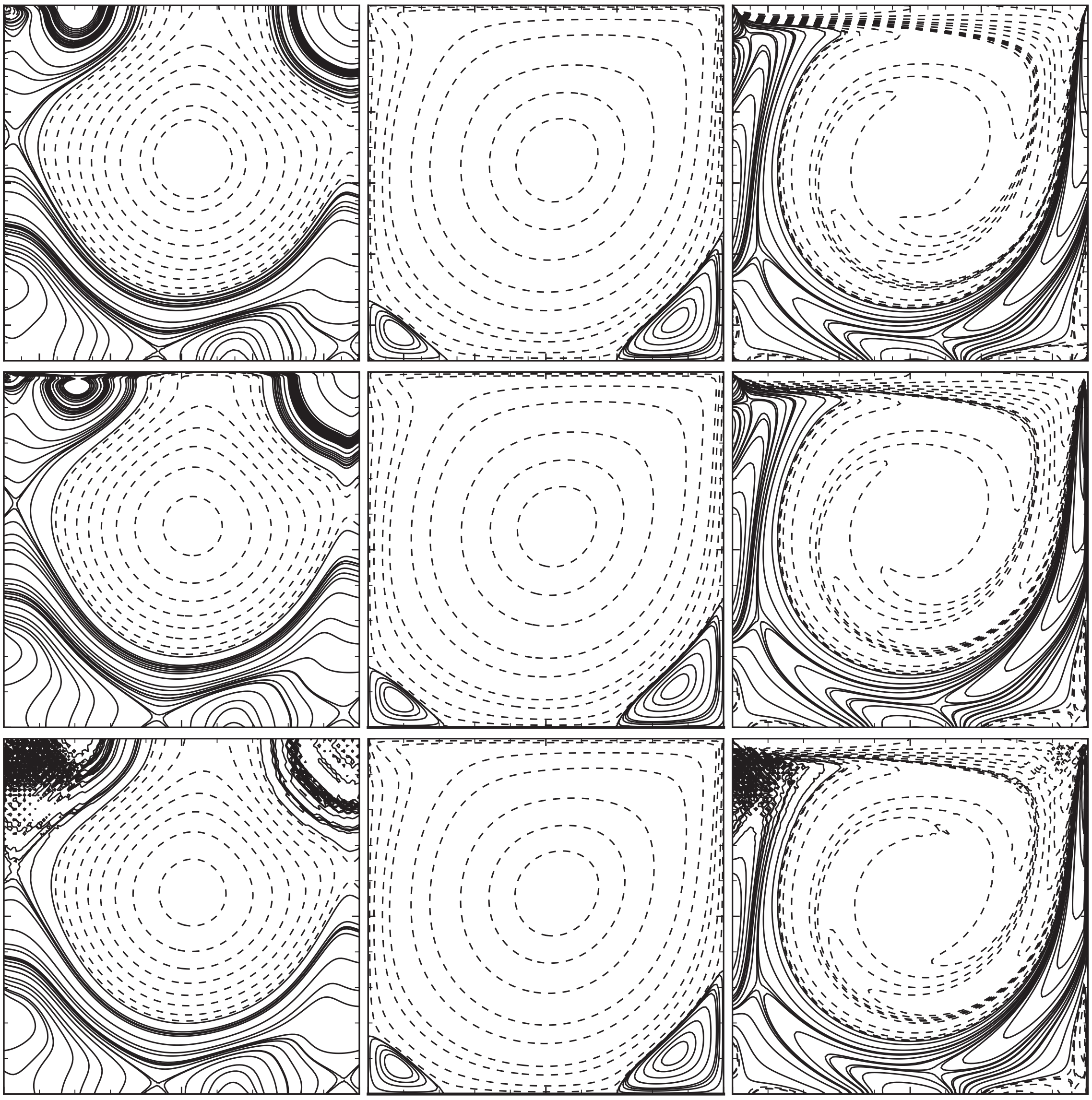

FIG. 3. Re = 1,000. Similar to Fig. 1.

are fixed by the Reynolds number Re [cf. Eq. (23)] and the BCs [cf. Eq. (11)], respectively. We fix $s_e = s_\nu = 1/\tau$ and vary s_ε in the following test. In addition to the case of $s_\varepsilon = 1.54$, which is the value used throughout this study unless otherwise stated, we also use $s_\varepsilon = 1.9$. In Fig. 6 we show the contour plot of the pressure field p and the vorticity field ω at the upper-left corner $(x, y) \in [0, 0.3] \times [0.7, 1.0]$ obtained by using the MRT-LBE with the resolution of $N^2 = 129^2$ and two different values of the relaxation rate $s_e = 1.64$ and $s_e = s_\nu$, and compared them with the TRT-LB and PS-MG results [18]. Bear in mind that in the TRT-LB scheme, $s_e = s_\varepsilon = s_\nu$. Because the MRT-LB results for $s_\varepsilon = 1.54$ and 1.9 are very close to each other, only the case of $s_\varepsilon = 1.54$ is shown in Fig. 6. Clearly, the relaxation rate s_e has no observable effect on the vorticity ω, but it affects the pressure p significantly. With $s_e = 1.64$, the contours of the pressure p near the top wall all exhibit a kink, which disappears with $s_e = s_\nu$ and with the TRT setting ($s_e = s_\varepsilon = s_\nu$). Our tests indicate that the pressure p is affected significantly by s_e and very little by s_ε.

To further investigate the pressure field near the wall, we show in Fig. 7 the pressure field near the top and the left walls at the fluid nodes adjacent to the boundary, for the case of Re = 1000. The fluid nodes adjacent to the top driving lid and the left wall are located at $y = \delta_x(1 - 1/2N)$ and $x = \delta_x/2N$, respectively; we assume that the no-slip BCs are satisfied at the line $\delta_x/2$ beyond the last fluid nodes, as discussed in Sec. II B. It can be seen clearly that, when $N = 65$, the pressure field p obtained by using the MRT-LBE with $s_e = 1.64$ has a kink near the top-left corner, where the velocity field is singular mathematically, while the pressure obtained with the TRT-LBE does not exhibit the kink. The kink may indicate that, with the particular choice of $s_e = 1.64$, the pressure field obtained by using the MRT-LBE oscillates near the top wall with a very short wavelength of about two grid spacings; and the

TABLE I. The center location (x, y), pressure p, stream function ψ, and vorticity ω of the primary vortex.

	N	(x, y)		p	ψ	ω
Re = 100						
PS	96	(0.615 753,	0.737290)	−0.077 912 93	−0.103 521 3	−3.168 830
MRT	65	(0.623 077,	0.746154)	−0.077 359	−0.103 303	−3.260 493
	129	(0.616 279,	0.740 310)	−0.077 366	−0.103 483	−3.182 492
	257	(0.616 732,	0.737 354)	−0.077 146	−0.103 514	−3.175 132
	513	(0.615 010,	0.737 817)	−0.077 238	−0.103 519	−3.162 855
TRT	65			−0.077 354	−0.103 300	−3.260 376
	129			−0.077 364	−0.103 482	−3.182 455
	257			−0.077 145		−3.175 125
	513					
ELBE	65			−0.077 528	−0.103 383	−3.273 133
	129			−0.077 305	−0.103 442	−3.189 044
	257			−0.077 029	−0.103 444	−3.180 179
	513			−0.077 112	−0.103 444	−3.167 593
LBGK	65	(0.607 692,	0.730 769)	−0.076 922	−0.103 434	−3.096 890
	129			−0.077 379	−0.103 490	−3.182 824
	257			−0.077 106	−0.103 494	−3.174 138
	513			−0.077 187	−0.103 493	−3.161 545
Re = 400						
PS	96	(0.554 100 3,	0.605 413 4)	−0.078 063 43	−0.113 9895	−2.292 390
MRT	65	(0.561 538,	0.607 692)	−0.076 940	−0.113 061	−2.286 839
	129	(0.554 264,	0.608 527)	−0.077 554	−0.113 838	−2.295 671
	257	(0.554 475,	0.605 058)	−0.077 635	−0.113 958	−2.295 325
	513	(0.554 581,	0.605 263)	−0.077 642	−0.113 983	−2.294 973
TRT	65			−0.077 077	−0.113 144	−2.288 611
	129			−0.077 558	−0.113 841	−2.295 716
	257					−2.295 318
	513			−0.077 641		−2.294 971
ELBE	65			−0.078 043	−0.114 145	−2.309 413
	129			−0.077 920	−0.114 031	−2.305 663
	257			−0.077 847	−0.114 000	−2.303 388
	513			−0.077 822	−0.113 994	−2.302 593
LBGK	65			−0.077 889	−0.114 159	−2.302 237
	129			−0.077 742	−0.114 022	−2.298 109
	257			−0.077 669	−0.113 991	−2.295 796
	513			−0.077 644	−0.113 985	−2.295 001
Re = 1000						
PS1	160	(0.5318,	0.5652)	—	−0.118 9366	−2.067 753
PS	96	(0.530 781 8,	0.565 232 5)	−0.081 441 73	−0.118 959 58	−2.068 611 8
MRT	65	(0.530 769,	0.561 538)	−0.070 758	−0.115 683	−2.031 164
	129	(0.531 008,	0.562 016)	−0.073 607	−0.118 406	−2.063 210
	257	(0.531 128,	0.562 257)	−0.074 010	−0.118 843	−2.067 339
	513	(0.531 189,	0.566 277)	−0.074 069	−0.118 919	−2.067 664
TRT	65			−0.071 975	−0.116 587	−2.047 911
	129			−0.073 711	−0.118 486	−2.064 605
	257			−0.074 014	−0.118 846	−2.067 397
	513					−2.067 661
ELBE	129			−0.074 672	−0.119 253	−2.081 538
	257			−0.074 461	−0.119 117	−2.077 452
	513			−0.074 422	−0.119 098	−2.076 384
LBGK	129			−0.074 361	−0.119 115	−2.073 356
	257			−0.074 134	−0.118 964	−2.069 077
	513			−0.074 092	−0.118 942	−2.067 992

TABLE II. The location (x, y), pressure p, stream function ψ, and vorticity ω of the secondary vortices.

	N	Lower-left secondary vortex				Lower-right secondary vortex			
					Re = 100				
		(x, y)	$p \times 10^2$	$\psi \times 10^6$	$\omega \times 10^2$	(x, y)	$p \times 10^2$	$\psi \times 10^5$	$\omega \times 10^2$
PS	96	(0.033 586, 0.034 560)	1.590 806	1.702 429	1.198 286	(0.943 043, 0.062 727)	1.935 636	1.273 8424	3.279 431
MRT	65	(0.038 462, 0.038 462)	1.6287	1.463 627	1.7232	(0.946 154, 0.069 231)	2.0320	1.226 275	3.4998
	129	(0.034 884, 0.034 884)	1.6424	1.787 060	1.4701	(0.941 860, 0.065 891)	2.0545	1.252 207	3.8814
	257	(0.036 965, 0.033 074)	1.6433	1.781 289	1.5448	(0.943 580, 0.064 202)	2.0585	1.269 040	3.6066
	513	(0.034 113, 0.034 113)	1.6470	1.793 627	1.4478	(0.942 495, 0.061 404)	2.0632	1.271 244	3.4830
TRT	65			1.462 137	1.7231		2.0318	1.225 926	3.4999
	129			1.786 233	1.4700		2.0544	1.252 060	3.8813
	257			1.781 069				1.269 009	
	513			1.793 598				1.271 239	
ELBE	65	(0.023 077, 0.038 462)	1.6508	1.037 024	0.4740		2.0366	1.110 408	3.4176
	129		1.6405	1.750 346	1.4632		2.0451	1.251 772	3.8433
	257		1.6372	1.854 699	1.5466		2.0458	1.292 095	3.5831
	513	(0.034 113, 0.036 062)	1.6411	1.894 922	1.5839	(0.942 495, 0.063 353)	2.0477	1.300 282	3.6342
LBGK	65	(0.023 077, 0.038 462)	1.6540	1.040 556	0.4753		2.0469	1.103 691	3.4493
	129		1.6435	1.756 372	1.4675		2.0553	1.245 085	3.8778
	257		1.6402	1.861 059	1.5512		2.0560	1.287 105	3.6159
	513	(0.034 113, 0.036 062)	1.6441	1.901 394	1.5886	(0.942 495, 0.063 353)	2.0579	1.295 183	3.6673
					Re = 400				
		(x, y)	$p \times 10^2$	$\psi \times 10^5$	$\omega \times 10^2$	(x, y)	$p \times 10^2$	$\psi \times 10^4$	$\omega \times 10$
PS	96	(0.0507 581, 0.0473 733)	3.561 592	1.411 438	6.095 086	(0.8854 916, 0.1223 319)	2.868 448	6.445 330	4.498 006
MRT	65	(0.053 846, 0.038 462)	3.547 8	1.276 588	3.717 3	(0.884 615, 0.130 769)	2.867 6	6.380 941	4.808 69
	129	(0.050 388, 0.050 388)	3.610 7	1.409 211	6.150 6	(0.887 597, 0.127 907)	2.928 6	6.434 737	4.636 41
	257	(0.048 638, 0.048 638)	3.621 4	1.425 964	5.638 0	(0.885 214, 0.122 568)	2.954 1	6.441 301	4.529 44
	513	(0.051 657, 0.047 758)	3.621 8	1.431 790	6.022 8	(0.885 965, 0.121 832)	2.957 2	6.444 459	4.451 15
TRT	65		3.554 7	1.280 803	3.714 0		2.867 9	6.415 618	4.796 49
	129		3.610 9	1.409 436	6.150 7		2.928 7	6.435 241	4.636 39
	257		3.621 3	1.425 921	5.638 0		2.954 0	6.441 246	4.529 41
	513			1.431775	6.0227			6.444 444	4.451 14
ELBE	65		3.630 4	0.898 6897	3.615 4		2.928 4	6.121 705	4.784 54
	129		3.625 0	1.315 058	6.088 0		2.923 3	6.409 993	4.564 71
	257		3.623 0	1.394 593	5.589 7		2.936 0	6.459 935	4.45056
	513		3.620 6	1.412 064	5.972 9	(0.884 016, 0.121 832)	2.939 2	6.473 385	4.490 90
LBGK	65		3.633 8	0.911 727 5	3.644 8		2.950 7	6.079 209	4.870 65
	129		3.626 6	1.333 206	6.139 3		2.944 2	6.377 187	4.646 69
	257		3.6244	1.412 786	5.635 9		2.957 0	6.430 523	4.531 12
	513		3.622 0	1.430 911	6.022 6		2.957 4	6.443 752	4.451 23
					Re = 1000				
		(x, y)	$p \times 10^2$	$\psi \times 10^4$	$\omega \times 10$	(x, y)	$p \times 10^2$	$\psi \times 10^3$	ω
PS1	160	(0.0833, 0.0781)	—	2.334 528	3.255 861	(0.8640, 0.1118)	—	1.729 717	1.109 789
PS	96	(0.083 276, 0.078 090)	3.846 69	2.334 089	3.544 582	(0.864 045, 0.111 815)	2.815 128	1.730 292	1.110 800
MRT	65	(0.084 615, 0.069 231)	4.2328	2.039 721	2.644 40	(0.869 231, 0.115 385)	3.3005	1.702 777	0.993 187
	129	(0.081 395, 0.081 395)	4.4558	2.278 163	3.584 90	(0.864 341, 0.112 403)	3.5013	1.730 337	1.086 797
	257	(0.083 658, 0.079 767)	4.4860	2.320 909	3.655 99	(0.861 868, 0.110 895)	3.5468	1.729 997	1.124 101
	513	(0.082 846, 0.078947)	4.4915	2.331 772	3.55657	(0.864 522, 0.112086)	3.5500	1.729 537	1.103 888
TRT	65		4.3129	2.069 050	2.66191	(0.853 846, 0.100 000)	3.3656	1.688 924	0.984 722
	129		4.4626	2.282 009	3.587 87		3.5043	1.731 326	1.085 883
	257		4.4862	2.321 087	3.656 14		3.5469	1.730 064	1.124 103
	513		4.4914	2.331 765	3.556 56			1.729 533	1.103 887
ELBE	129		4.5203	2.212 502	3.581 11		3.5382	1.705 555	1.074 814
	257		4.5064	2.268 905	3.635 86		3.5396	1.718 036	1.104 222
	513		4.5044	2.284222	3.53476		3.5367	1.720 601	1.111 817
LBGK	129		4.5106	2.260 153	3.605 05		3.5573	1.713 561	1.096 735
	257		4.4954	2.316 249	3.659 19		3.5577	1.725 431	1.126 455
	513		4.4932	2.330 706	3.557 06		3.5522	1.728 455	1.104 395

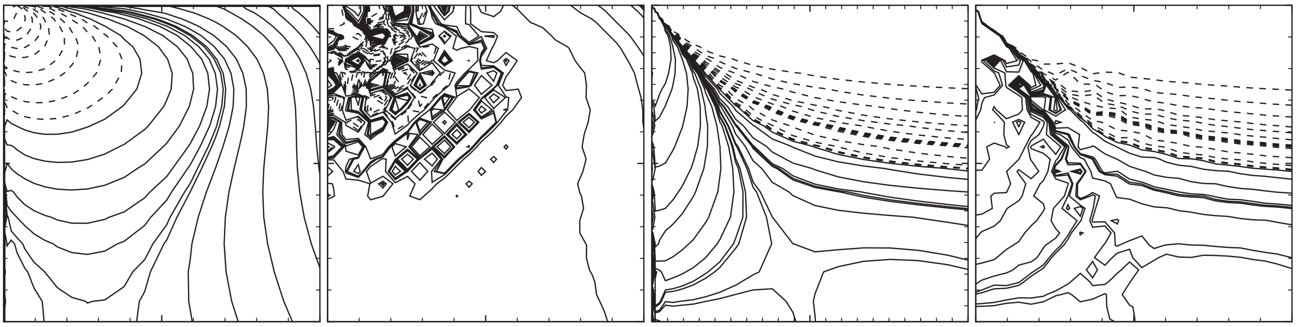

FIG. 4. The pressure field p (two figures on the left) and the vorticity field ω (two figures on the right) at the upper left corner $(x, y) \in [0, 0.1] \times [0.9, 1.0]$, Re = 1000. From left to right: p obtained using the PS method ($N = 96$) and the ELBE scheme ($N^2 = 257^2$) and ω obtained using the PS method and the ELBE scheme.

oscillations quickly attenuate. We observe that, with the choice of $s_e = s_\nu$ and $s_\varepsilon = 1.54$ (or 1.9), the kink in the pressure field near the top wall disappears completely. Note that, for $\mathrm{Re} = 1000$, both the ELBE and LBGK schemes diverge with the resolution $N = 65$. For $N = 129$ and 257, the pressure field obtained with the ELBE exhibits strong oscillations near the top-left corner, and the magnitude of the oscillations is reduced as N increases while the Reynolds number is fixed. This is understandable because with Re fixed, the value of τ increases linearly as N increases, and so do the viscosity ν and the dissipation to the density fluctuations in the system, as indicated by Eq. (23).

We also study the velocity field $\boldsymbol{u}$ and its gradient $\nabla\boldsymbol{u}$ near the walls. In Fig. 8 we show the gradient of the tangential velocity u along the transverse direction, $\partial_y u(x, y)$, and the transverse velocity $v(x, y)$ for $\mathrm{Re} = 1000$ at the fluid nodes adjacent to the driving lid, that is, $y = (1 - 1/2N)$, for $N = 65$, 129, and 257. Instead of showing $u(x, y)$ near the top wall, we choose to show $\partial_y u(x, y)$ for it illustrates more clearly the differences between the results obtained by using different methods. The tangential velocity near the top wall, u, has a very sharp gradient in the y direction near the top corners, which are captured by the MRT-LB and TRT-LB schemes, and as the resolution N increases, the velocity fields obtained by the MRT-LB and TRT-LB schemes agree with the PS-MG result better and better. The velocity field obtained by using the ELBE oscillates severely near the wall. Similar to the pressure field, oscillations are weakened as N increases.

In Fig. 9 we show $\partial v(x, y)/\partial x$ and $u(x, y)$ near the left wall at $x = \delta_x/2N$ for $N = 65$, 129, and 257. Similar to the results shown in Fig. 8, the velocity field $\boldsymbol{u}$ obtained by using the ELBE scheme exhibits oscillations near the top-left corner, while the velocity field obtained by using the MRT-LB and TRT-LB schemes does not show any oscillation.

It should be emphasized that, for the ELBE and LBGK schemes with one relaxation time and the BB-type of BCs, it is impossible to achieve converging results as the mesh is refined because of inaccurate BCs. The inaccurate BCs can lead to severe adverse effects (cf., e.g., [48]). To substantiate this point, we compute the positions where the no-slip BCs are satisfied in the simulations in the middle one-third sections of the left (L), bottom (B), and right (R) walls; that is, we compute the distance δ between the last fluid nodes to the locations where $\boldsymbol{u} = \boldsymbol{0}$, which is derived from Eq. (19b):

$$\delta = \frac{1}{2} + \sqrt{H_{1/2}^2 + 4\Delta^2 - 1} - H_{1/2}. \tag{29}$$

For the Poiseuille flow, $\Delta = 1/2$; thus, $\delta = \delta_x/2$ exactly. We use a parabola to fit the velocity tangential to a wall with three points adjacent to the boundary and on the grid line normal to the wall. The least-square fitted parabola is then extrapolated to find the position where the tangential velocity is equal to zero. We observe that in the middle one-third section of the walls, the tangential velocity is at least two orders of magnitude larger than the transverse velocity. In the ideal situation, that is, the

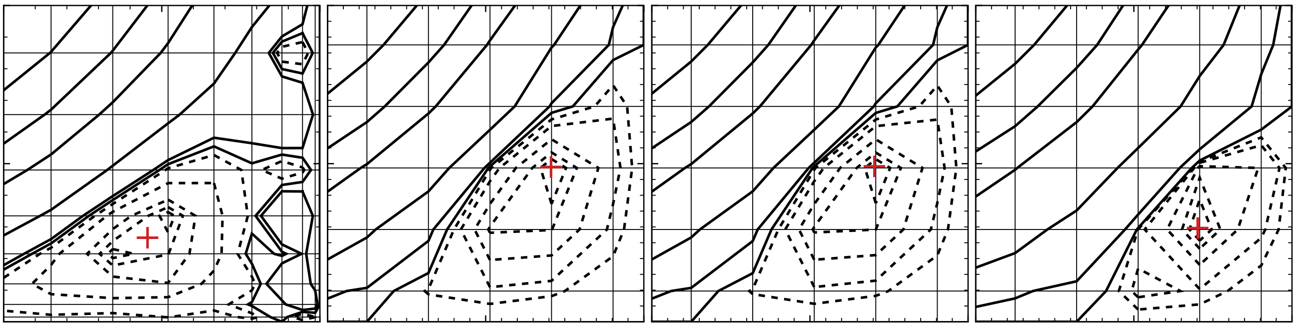

FIG. 5. (Color online) The stream function ψ at the lower-right corner $(x, y) \in [0.98, 1] \times [0, 0.02]$, Re = 1000. From left to right: PS-MG method ($N = 96$) [18], MRT-LBE, TRT-LBE, and ELBE ($N = 257$). The tertiary vortex is clearly seen. The straight horizontal and vertical lines are the grid lines. The symbol "+" marks the approximated position of the tertiary vortex center.

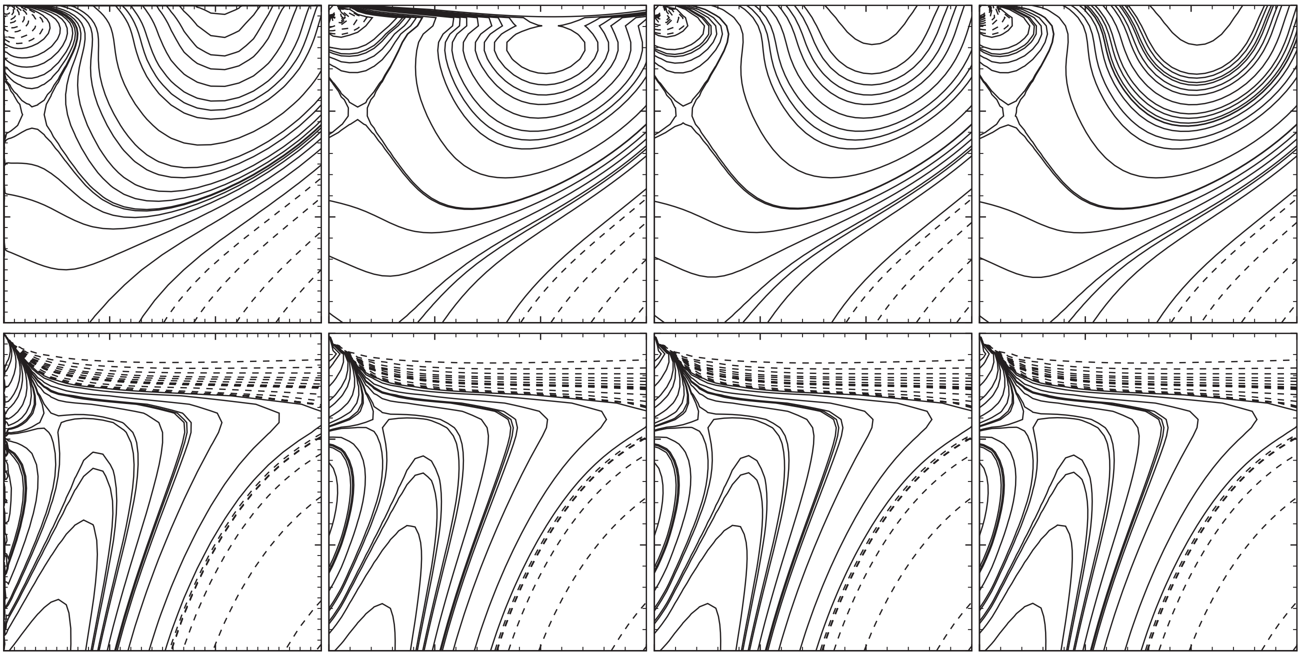

FIG. 6. The pressure field p (top) and the vorticity field ω (bottom) at the upper-left corner $(x, y) \in [0, 0.3] \times [0.7, 1.0]$, Re = 1000. From left to right: the PS-MG method ($N = 96$) [18], the MRT-LBE with $s_e = 1.64$ and $s_e = s_\nu$, and the TRT-LBE ($N = 129$).

Poiseuille flow, $\delta = \delta_x/2$. We fix the mesh size $N^2 = 65^2$ and 129^2 and vary the value of the viscosity ν (or the relaxation parameter τ). The results are summarized in Table IV.

In Table IV we present the mean value $\bar{\delta}$, the maximum value δ_{M}, and the minimum value δ_{m}, of δ along the left (L), bottom (B), and right (R) walls. Clearly, the value of δ computed by using the MRT-LB and TRT-LB schemes varies very little—at the worst scenario the value of δ deviates from $\delta_x/2$ less than 6%. In contrast, the value of δ obtained by using the ELBE and LBGK schemes can be greater than $3.7\delta_x$, which is more than three grid spacings away from the assumed boundary location.

To further illustrate the inaccuracy of the ELBE and LBGK schemes with the BB BCs, we use the following formula [34] to fit the tangential velocity along center lines of the cavity,

$$u_i = \frac{4U_*}{N_*^2} i(N_* - i) + U_{\mathrm{s}}, \tag{30a}$$

$$U_{\mathrm{s}} = \frac{2U_*}{3N_*^2} \left[(2\tau - 1)(4\tau - 3) - 3N_*\right], \tag{30b}$$

where U_* and N_* are the effective maximum velocity and channel width, respectively, which are to be determined by the least-square fitting. For the MRT-LB and TRT-LB schemes, the corresponding formula is

$$u_i = \frac{4U_*}{N_*^2}(i - 1/2)(N_* + 1/2 - i). \tag{31}$$

TABLE III. The center location (x, y), pressure p, stream function ψ, and vorticity ω of the tertiary vortex at the lower-right corner.

	N	(x, y)	$p \times 10^2$	$\psi \times 10^8$	$\omega \times 10^3$
PS1	160	(0.992 32, 0.007 65)	—	−5.03944	—
PS	96	(0.989 13, 0.005 34)	2.84	−6.00	8.91
	129	(0.996 12, 0.003 87)	3.51	−0.976	0.674
MRT	257	(0.994 16, 0.009 72)	3.55	−4.03	4.84
	129	(0.996 12, 0.003 87)	3.52	−0.781	0.606
TRT	257	(0.994 16, 0.009 72)	3.56	−4.07	4.91
ELBE	257	(0.994 16, 0.005 83)	3.55	−0.937	0.535

We use a small mesh of size $N^2 = 33^2$ and $\tau = 3.0$, which means very small Reynolds number. The tangential velocities along the horizontal center line ($y = 1/2$) near the left wall ($x = 0$) and along the vertical center line ($x = 1/2$) near the bottom wall ($y = 0$) are fitted with Eqs. (30a) and (31). The results are shown in Fig. 10.

The results shown in Fig. 10 indicate that, when the flow is laminar, the tangential velocity near the wall is accurately represented by a parabola when the transverse velocity is small enough, that is, when the location is sufficiently away from the corners so the nonlinear term $\boldsymbol{u}\cdot\boldsymbol{\nabla}\boldsymbol{u}$ is sufficiently small. The result also suggests that, with U and Re fixed, the velocity field obtained by using the ELBE or LBGK scheme with the BB BCs will not converge when the resolution N increases. This is because τ increases linearly with N [cf. Eq. (23)], and for the SRT collision models with the BB BCs, $\Delta = 12\nu^2 = 12(NU/\mathrm{Re})^2$ [cf. Eq. (19b)]; therefore, the location where $\boldsymbol{u} = \boldsymbol{0}$ is satisfied will move further and further away from the last fluid nodes as N increases.

To further substantiate this point, we compute the τ dependence of the slip velocity U_{s} on the boundary node at the center of the bottom wall by using the ELBE scheme with $N = 33$. For a given value of τ, we can fit the velocity tangential to the wall with a parabola which includes two parameters, the effective maximum velocity U_* and the effective channel width N_*, as the results shown in Fig. 10.

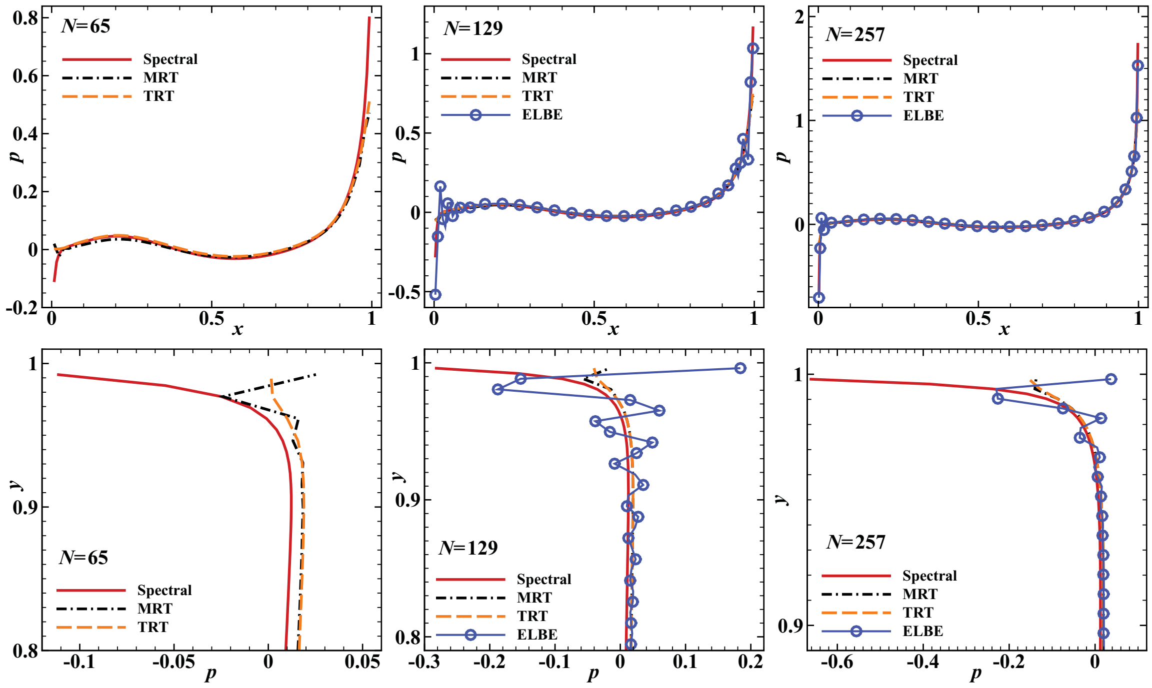

FIG. 7. (Color online) The pressure field near the top (top row) and the left (bottom row) walls, Re = 1000.

The velocity profile is then extrapolated to the boundary node to obtain the effective slip velocity U_s, which is compared with the value of U_s computed from Eq. (30b). As shown in Fig. 11, clearly, the τ dependence of U_s/U_* in the cavity flow is well predicted by Eq. (30b), which is exact for the Poiseuille flow. Therefore, to achieve convergence by using the SRT-LB schemes, that is, the ELBE and LBGK schemes, with the BB BCs, one must maintain a constant ν with a fixed Re in order to control the error due to inaccurate BCs, which means the product UN must be kept as a constant so U must decrease as $1/N$ when the resolution N increases. Consequently, the number of iterations for the SRT-LB schemes to attain steady state would grow as $\mathrm{Re}N^2$, as opposed to $\mathrm{Re}N/U$ for the MRT-LB schemes with U kept as a constant.

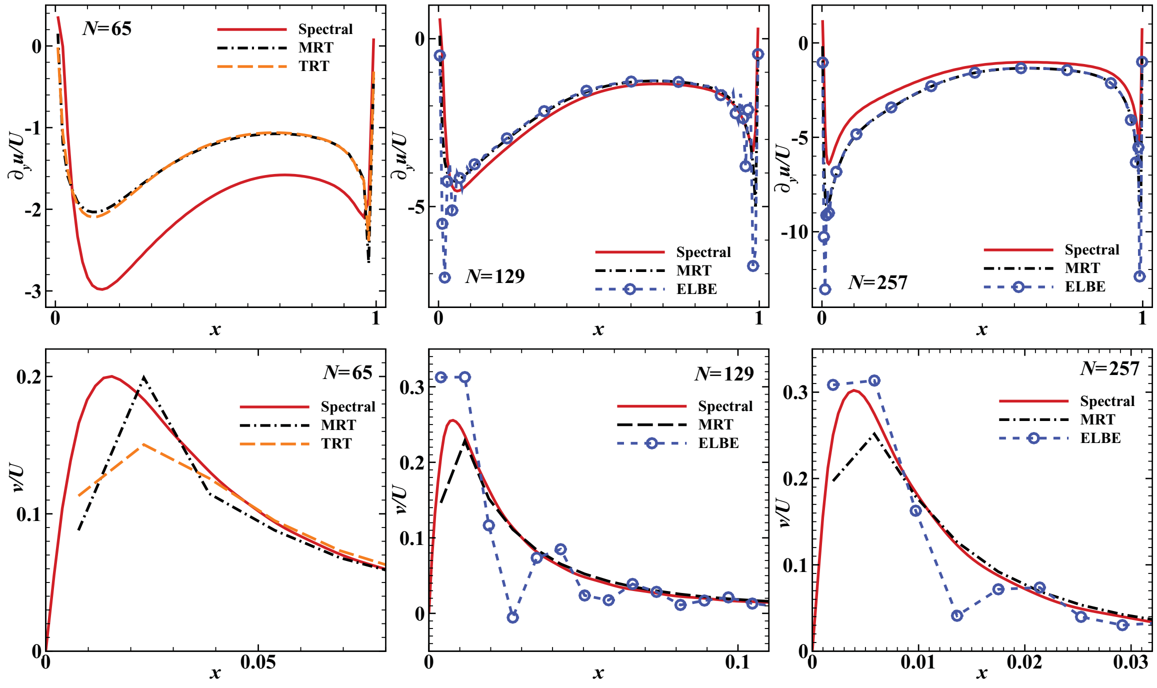

FIG. 8. (Color online) The velocity field $\boldsymbol{u} = (u, v)$ at the last fluid nodes located at $y = 1 - 1/2N$ and adjacent to the top wall, Re = 1000. $\partial u(x, y)/\partial y$ (top row) and $v(x, y)/U$ (bottom row) at (from left to right) $y = 129/130$, $y = 257/258$, and $y = 513/514$.

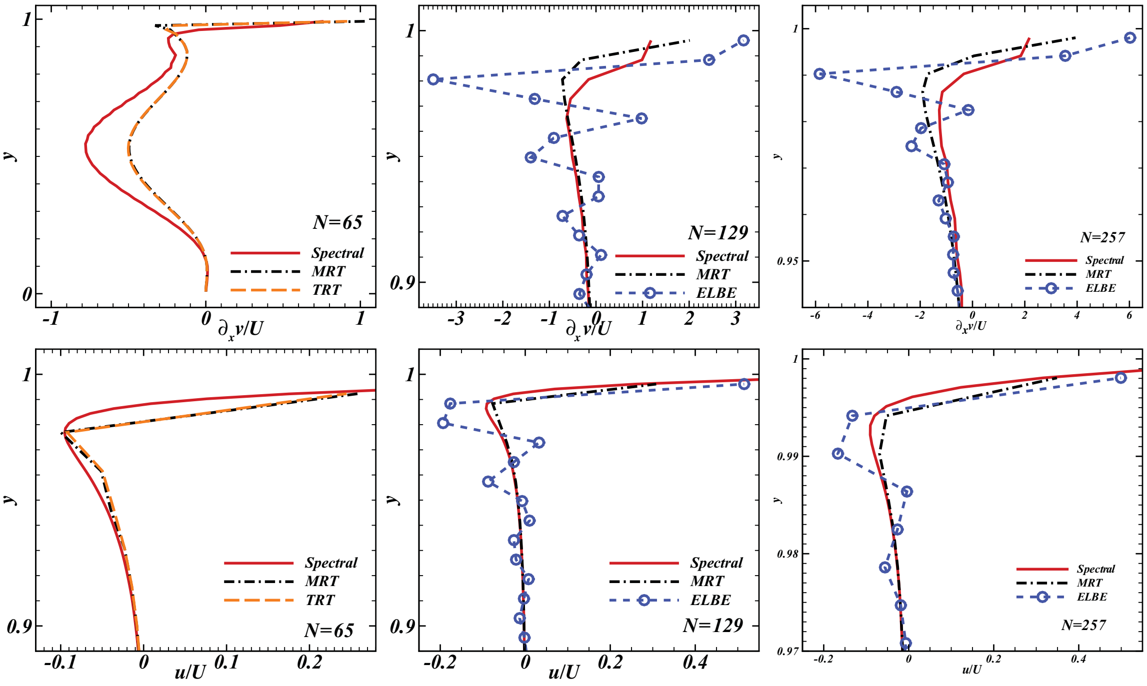

FIG. 9. (Color online) The velocity field at the last fluid nodes located at $x = 1/2N$ and adjacent to the left wall, Re $= 1000$. (Top row) $\partial v(x, y)/\partial x$ and (bottom row) $u(x, y)$ at (from left to right) $x = 1/130$, $x = 1/258$, and $x = 1/514$.

Our results shown in Table IV and Figs. 10 and 11 unequivocally demonstrate that the so-called slip velocity U_s obtained by using the ELBE and LBGK schemes is merely a numerical artifact of these models due to their inaccurate BCs. The slip velocity obtained by using any scheme based on the SRT model, such as the ELBE and LBGK ones, cannot converge as N increases with fixed Re, Ma, and Kn; hence, it is N dependent. In fact, for most ELBE and LBGK simulations of flow through a microchannel [35–37,49], the resolution N is indeed used as a fitting parameter, and such results are erroneous and flawed, as pointed out previously [38,39,41,50]. On the other hand, the MRT-LBE is free of the inherent defects of the SRT model and is capable of reproducing convergent results [41].

D. Accuracy and convergence

We now study the convergence behavior of the LB schemes. For the Reynolds number Re $= 100$, 400, and 1000, the mesh resolutions, N^2, used for the LB simulations are 65^2, 129^2, 257^2, and 513^2. We first compute the total energy E and the total enstrophy Z of the system:

$$E = \frac{\frac{1}{2}\int_\Omega \|\boldsymbol{u}(\boldsymbol{x})\|^2\, d\boldsymbol{x}}{\int_\Omega d\boldsymbol{x}} = \frac{\frac{1}{2}\sum_i \|\boldsymbol{u}(\boldsymbol{x}_i)\|^2}{N^2}, \tag{32a}$$

$$Z = \frac{\frac{1}{2}\int_\Omega \omega^2(\boldsymbol{x})\, d\boldsymbol{x}}{\int_\Omega d\boldsymbol{x}} = \frac{\frac{1}{2}\sum_i \omega^2(\boldsymbol{x}_i)}{N^2}, \tag{32b}$$

where Ω is the entire flow domain, and both the velocity $\boldsymbol{u}$ and the vorticity ω have been properly normalized by U and L/U, respectively. We also compute the L^2-normed error for the velocity field, $\boldsymbol{u}_N(\boldsymbol{x}_i)$, obtained by using an LB scheme with a given mesh resolution N^2,

$$E_2(\boldsymbol{u}_N) := \frac{\sum_i \|\boldsymbol{u}_N(\boldsymbol{x}_i) - \boldsymbol{u}_*(\boldsymbol{x}_i)\|_2}{\sum_i \|\boldsymbol{u}_*(\boldsymbol{x}_i)\|_2}, \tag{33}$$

where $\boldsymbol{u}_*(\boldsymbol{x}_i)$ denotes the reference field. Two reference fields are used: the LB solution obtained with the largest mesh resolution of $N = 513$ and the PS-MG solution with $N = 96$.

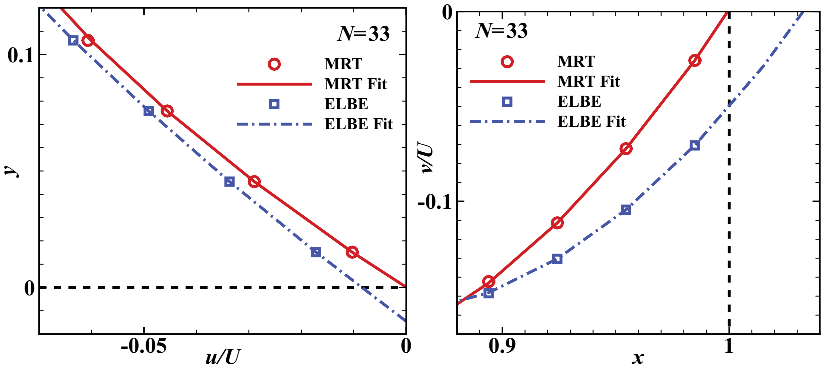

FIG. 10. (Color online) The tangential velocities near the bottom wall (left) and the right wall (right), $N^2 = 33^3$ and $\tau = 3.0$. The symbols are data obtained in simulations, and the dash-dotted and solid lines correspond to Eqs. (30a) and (31), respectively. The straight dashed lines mark the assumed locations of the bottom wall $x = 0$ and the right wall $y = 1$.

TABLE IV. The distance (δ) of the last fluid node to the boundary wall, where $\boldsymbol{u} = \boldsymbol{0}$. L, B, and R indicate the left, bottom, and right wall, respectively. $\bar{\delta}$, δ_{M}, and δ_{m} denote the averaged, maximum, and minimum values of δ in the middle one-third of a wall, respectively.

		$\tau = 0.55$			$\tau = 1.0$			$\tau = 3.0$			$\tau = 5.0$		
		$\bar{\delta}$	δ_{M}	δ_{m}	$\bar{\delta}$	δ_{M}	δ_{m}	$\bar{\delta}$	δ_{M}	δ_{m}	$\bar{\delta}$	δ_{M}	δ_{m}
								$N^2 = 65^2$					
MRT	L	0.5039	0.5076	0.4979	0.4993	0.4996	0.4985	0.4986	0.4989	0.4980	0.4985	0.4989	0.4977
	B	0.5047	0.5084	0.4985	0.5023	0.5026	0.5017	0.5021	0.5024	0.5016	0.5021	0.5024	0.5016
	R	0.4774	0.4789	0.4719	0.4970	0.4974	0.4964	0.4982	0.4984	0.4979	0.4984	0.4987	0.4980
TRT	L	0.5035	0.5063	0.4985	0.4992	0.4996	0.4983	0.4983	0.4986	0.4975	0.4982	0.4985	0.4973
	B	0.5043	0.5075	0.4988	0.5025	0.5028	0.5019	0.5024	0.5027	0.5020	0.5024	0.5027	0.5019
	R	0.4810	0.4824	0.4742	0.4966	0.4970	0.4960	0.4979	0.4981	0.4976	0.4980	0.4982	0.4976
ELBE	L	0.4838	0.5035	0.4783	0.5024	0.5030	0.5007	0.8748	1.1081	0.7056	2.6185	3.7490	1.9473
	B	0.4983	0.5152	0.4934	0.5052	0.5057	0.5040	0.7535	0.7683	0.7243	1.3025	1.3169	1.2678
	R	0.5070	0.5585	0.4745	0.4985	0.5004	0.4966	0.8928	1.1051	0.7356	2.7151	3.6252	2.1112
LBGK	L	0.4838	0.5034	0.4783	0.5024	0.5030	0.5007	0.8748	1.1086	0.7053	2.6174	3.7351	1.9495
	B	0.4979	0.5138	0.4932	0.5051	0.5058	0.5042	0.7537	0.7685	0.7246	1.3027	1.3171	1.2682
	R	0.5069	0.5580	0.4745	0.4984	0.5004	0.4965	0.8923	1.1045	0.7353	2.7225	3.6500	2.1121
								$N^2 = 129^2$					
MRT	L	0.5010	0.5039	0.4975	0.5000	0.5001	0.4996	0.4996	0.4998	0.4993	0.4996	0.4997	0.4993
	B	0.5015	0.5043	0.4973	0.5006	0.5010	0.5001	0.5006	0.5008	0.5002	0.5006	0.5009	0.5003
	R	0.4896	0.4919	0.4617	0.4988	0.4990	0.4983	0.4994	0.4995	0.4991	0.4995	0.4996	0.4992
TRT	L	0.5009	0.5033	0.4980	0.5000	0.5002	0.4996	0.4996	0.4997	0.4993	0.4995	0.4997	0.4993
	B	0.5014	0.5036	0.4977	0.5007	0.5010	0.5003	0.5007	0.5010	0.5003	0.5006	0.5009	0.5004
	R	0.4909	0.4933	0.4642	0.4987	0.4990	0.4981	0.4993	0.4994	0.4991	0.4994	0.4995	0.4992
ELBE	L	0.4886	0.4984	0.4848	0.5018	0.5021	0.5011	0.6369	0.6981	0.5754	1.0796	1.4689	0.8005
	B	0.4982	0.5113	0.4922	0.5020	0.5025	0.5014	0.6366	0.6466	0.6140	0.9287	0.9546	0.8688
	R	0.5387	0.8978	0.4899	0.4986	0.5003	0.4968	0.6115	0.6911	0.5439	1.0715	1.4629	0.7890
LBGK	L	0.4886	0.4985	0.4848	0.5019	0.5021	0.5012	0.6367	0.6978	0.5754	1.0794	1.4690	0.8003
	B	0.4979	0.5114	0.4919	0.5020	0.5025	0.5014	0.6367	0.6468	0.6138	0.9290	0.9549	0.8694
	R	0.5385	0.9117	0.4898	0.4987	0.5003	0.4971	0.6112	0.6907	0.5435	1.0709	1.4626	0.7884

When the PS-MG solution is used as the reference solution, it is interpolated to the equispaced mesh of size N^2 used in the LB simulations. The above formula can also be applied to the vorticity and pressure fields. We can also estimate the convergence speed α as the following:

$$\alpha \approx \frac{\ln\left[E_2(\boldsymbol{u}_M)/E_2(\boldsymbol{u}_N)\right]}{\ln(N/M)}, \tag{34}$$

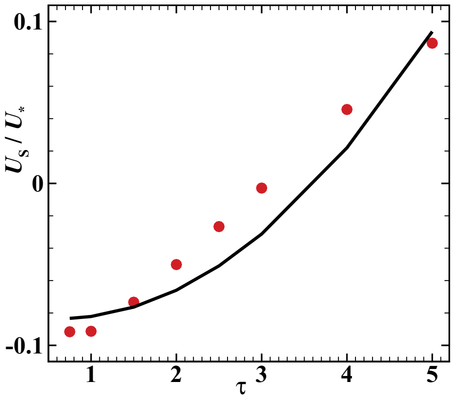

FIG. 11. (Color online) The τ dependence of the tangential velocity U_s at the boundary node at the center of the bottom wall. $N^2 = 33^2$. The symbols and the solid line are data obtained by using the ELBE scheme and Eqs. (30a), respectively.

where $E_2(\boldsymbol{u}_M)$ and $E_2(\boldsymbol{u}_N)$ are the errors with the resolution M and N, respectively. In what follows, we use the errors with two largest meshes to compute α.

When computing the total energy E and the total enstrophy Z, the integrations of $\boldsymbol{u}\cdot\boldsymbol{u}/2$ and $\omega^2/2$ are carried out over the entire flow domain Ω or only the fluid nodes, that is, excluding the boundary $\partial\Omega$. When the boundary $\partial\Omega$ is included in the integration, the integrand is weighted with a factor of $1/2$ and $1/4$ at $\partial\Omega$ and the four concerns, respectively, because the boundary is only $\delta_x/2$ away from the nearest fluid nodes. The Clenshaw-Curtis quadrature formula for integration is used to compute E and Z from the flow field obtained by using PS-MG method [18].

In Table V we present the total energy E integrated over Ω and $\Omega\backslash\partial\Omega$. Several observations can be made. First of all, the value of E computed on the entire flow domain Ω decreases monotonically as N increases, while the value of E computed on fluid nodes alone, that is, on $\Omega\backslash\partial\Omega$, increases monotonically, hence providing the upper and lower bounds of E, respectively. The lower and upper bounds obtained by the LB schemes with $N = 513$ have two or three significant digits agreeing with the PS-MG values, and the lower bounds are generally closer to the PS-MG values. This clearly indicates that the BCs have considerable influence on the value of E. Second, the lower and upper bounds of E converge differently. The convergence speed for the upper bounds is about 1.0, independent of the LB scheme, as shown by the left panel of

TABLE V. The total energy E on the entire flow domain Ω or only the interior, that is, the flow domain excluding the boundary $\Omega\backslash\partial\Omega$. The case of $N = 96$ is obtained by using the PS-MG method and the Clenshaw-Curtis quadrature formula for integration [18].

	E on Ω				E on $\Omega\backslash\partial\Omega$			
N	MRT	TRT	ELBE	LBGK	MRT	TRT	ELBE	LBGK
$\mathrm{Re} = 100$								
65	0.035 838	0.035 837	0.035 968	0.036 017	0.034 173	0.034 171	0.034 311	0.034 363
129	0.035 223	0.035 222	0.035 185	0.035 234	0.034 371	0.034 370	0.034 332	0.034 383
257	0.034 855	0.034 855	0.034 770	0.034 820	0.034 424	0.034 424	0.034 337	0.034 388
513	0.034 655	0.034 655	0.034 556	0.034 606	0.034 438	0.034 438	0.034 338	0.034 389
96	0.0344435487							
$\mathrm{Re} = 400$								
65	0.041 307	0.041 357	0.042 193	0.042 239	0.039 983	0.040 036	0.040 925	0.040 974
129	0.041 299	0.041 301	0.041 444	0.041 474	0.040 637	0.040 639	0.040 786	0.040 817
257	0.041 108	0.041 107	0.041 111	0.041 140	0.040 774	0.040 773	0.040 778	0.040 807
513	0.040 972	0.040 972	0.040 945	0.040 974	0.040 804	0.040 804	0.040 778	0.040 806
96	0.0408141964							
$\mathrm{Re} = 1000$								
65	0.043 148	0.043 708	—	—	0.041 939	0.042 534	—	—
129	0.044 602	0.044 656	0.045 221	0.045 181	0.044 043	0.044 099	0.044 681	0.044 641
257	0.044 704	0.044 707	0.044 861	0.044 809	0.044 426	0.044 429	0.044 586	0.044 533
513	0.044 638	0.044 638	0.044 711	0.044 658	0.044 499	0.044 499	0.044 573	0.044 519
96	0.044 528 639 9							

Fig. 12. However, the convergence speed for the lower bounds is scheme dependent. For the MRT-LB and TRT-LB schemes, the convergence speed is about 2.0; and the ELBE and LBGK schemes cease to converge when $N \geqslant 129$, as shown by the right panel of Fig. 12. This clearly indicates the importance of the BCs and demonstrates the superiority of the MRT-LB and TRT-LB schemes over the ELBE and LBGK schemes. The inaccuracy of the BCs in the ELBE and LBGK schemes severely degrades the quality of the velocity field, as shown in the previous section, which, in turn, negatively affects the quality of integral quantities in the system, such as E. A similar observation has made previously (cf., e.g., [48]).

In Table VI we present the values of the total enstrophy Z computed over the entire fluid domain Ω or only on the fluid nodes $\Omega\backslash\partial\Omega$, similar to the total energy E in Table V. Because the vorticity $\omega = \nabla \times \boldsymbol{u}$ is singular on the top corners, we should not expect ω computed with finite-difference to converge as N increases. Indeed, Z does not seem to converge when it is computed with the boundary value, while Z obtained by integrating over the fluid nodes alone appears to converge to the corresponding values obtained by using the PS-MG method with the convergence speed approximately equal to 1.0.

In Table VII we show the L^2-normed errors for the velocity field $\boldsymbol{u}$, the vorticity field ω, and the pressure field p, with the reference fields obtained by a particular LB scheme with the largest mesh size $N^2 = 513^2$. This is a consistency test to see if the solution of each LB scheme converges when mesh is refined. It should be pointed out that the grid points on two different meshes are not perfectly laying on top of each other because the boundary is only $\delta_x/2$ away from the fluid nodes adjacent to the boundary. This introduces a systematic error when it is assumed that the grid points on two meshes are perfectly aligned with each other. The alternative would be to interpolate data in one mesh to the grid points of the other mesh. This would introduce the error due to interpolations. We use the former approach, that is, assuming the grid points on two meshes are aligned with each other, because it is simpler.

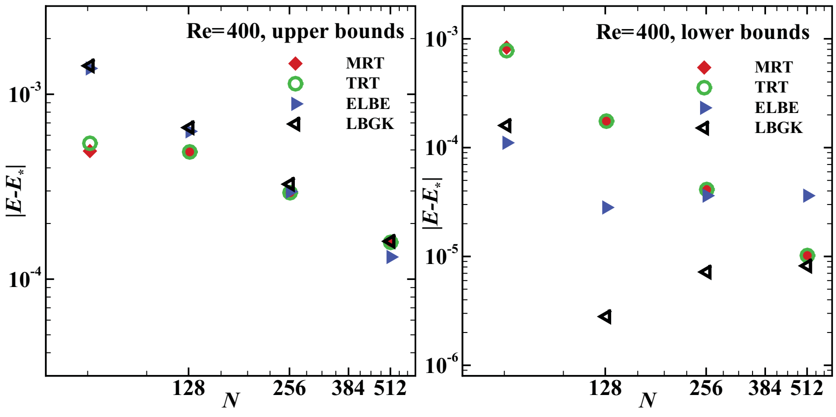

FIG. 12. (Color online) The convergence behaviors of the upper and lower bounds of the total energy E in Table V. $\mathrm{Re} = 400$.

TABLE VI. The total enstrophy Z on the entire flow Ω or only the interior fluid nodes $\Omega\backslash\partial\Omega$. The case of $N = 96$ is obtained by using the PS-MG method [18].

	Z on Ω				Z on $\Omega\backslash\partial\Omega$			
N	MRT	TRT	ELBE	LBGK	MRT	TRT	ELBE	LBGK
				Re = 100				
65	13.871 481	13.873 742	13.454 383	13.446 956	9.269 805	9.274 383	9.241 040	9.251 079
129	15.482 982	15.488 585	15.427 444	15.397 035	10.750 270	10.760 709	10.739 797	10.745 891
257	17.029 284	17.037 512	17.887 833	17.814 132	12.230 504	12.244 964	12.430 537	12.422 978
513	18.530 581	18.540 718	21.699 074	21.544 143	13.700 707	13.717 798	14.644 868	14.603 368
96				17.477 303 683 7				
				Re = 400				
65	17.742368	17.736531	16.868321	16.886885	11.825388	11.821156	12.095108	12.129003
129	19.037842	19.036509	18.393694	18.395769	13.470404	13.467743	13.525332	13.558239
257	20.300225	20.302552	19.875573	19.842928	15.017366	15.021890	14.965177	14.991985
513	21.604582	21.610247	21.598736	21.511861	16.510269	16.520684	16.491830	16.504690
96				20.2966851756				
				Re = 1000				
65	23.821075	23.685784	—	—	15.291749	15.293886	—	—
129	24.687357	24.670743	23.508602	23.543192	17.348414	17.344816	17.595882	17.656577
257	25.466743	25.464046	24.721660	24.728690	19.089853	19.085165	19.169924	19.227861
513	26.384755	26.385888	25.887249	25.846128	20.662131	20.664337	20.606352	20.654849
96				24.4937074969				

The data in Table VII show that the convergence speed α for the velocity $\boldsymbol{u}$ and the vorticity ω is approximately 1.5 and 1.0, respectively, independent of the Reynolds number Re. As for the pressure p, the convergence speed depends not only on the Reynolds number Re, but also on the scheme. For the MRT-LB and TRT-LB schemes, the convergence speed for p increases from about 1.0 at Re = 100 to about 1.5 at Re = 1000. For the ELBE and LBGK schemes, the trend is the opposite: The convergence speed decreases from about 1.5 at Re = 100 to about 1.0 at Re = 1000. Given the singular nature of the flow, the convergence speeds for $\boldsymbol{u}$, ω, and p observed here are those of a second-order scheme and consistent with the theory [29].

In Table VIII we show the L^2-normed errors by using the PS-MG solutions with $N = 96$ [18] as the reference fields in Eq. (33). The errors are computed over the entire flow domain Ω, that is, including the boundary $\partial\Omega$. We note that the errors between the LB and PS-MG solutions are smaller in general than those in Table VII, except some isolated cases: the velocity field $\boldsymbol{u}$ computed by using the ELBE scheme at Re = 400 and 1000 and the pressure field at Re = 1000. This suggests that the systematic error due to mismatched grid points in the LB

TABLE VII. Convergence of the LB simulations. The reference fields in Eq. (33) are obtained by using the LB schemes with the largest mesh size $N^2 = 513^2$. For Re = 1000, both the ELBE and LBGK schemes are unstable when $N = 65$. The rows denoted with "α" are the convergence speed.

	$E_2(\boldsymbol{u})$				$E_2(\omega)$				$E_2(p)$			
N	MRT	TRT	ELBE	LBGK	MRT	TRT	ELBE	LBGK	MRT	TRT	ELBE	LBGK
						Re = 100						
65	0.086 320	0.086 237	0.075 633	0.075 838	0.813 140	0.813 394	0.806 760	0.810 152	0.823 758	0.834 287	0.585 283	0.585 244
129	0.038 947	0.038 782	0.033 147	0.033 222	0.595 578	0.595 863	0.602 381	0.605 486	0.622 870	0.638 575	0.347 275	0.347 390
257	0.013 212	0.013 132	0.011 064	0.011 084	0.294 511	0.298 272	0.330 958	0.330 293	0.300 127	0.314 486	0.132 029	0.132 087
α	1.55	1.56	1.58	1.58	1.01	0.99	0.86	0.87	1.05	1.02	1.39	1.39
						Re = 400						
65	0.100 600	0.100 410	0.088 230	0.088 508	0.797 194	0.798 397	0.796 002	0.799 037	0.663 377	0.684 981	0.594 142	0.593 535
129	0.043 847	0.043 818	0.040 090	0.040 255	0.571 285	0.572 026	0.568 732	0.572 676	0.407 075	0.426 939	0.345 349	0.345 294
257	0.014 651	0.014 628	0.013 630	0.013 693	0.275 600	0.278 278	0.277 395	0.277 874	0.160 402	0.170 074	0.124 284	0.124 413
α	1.58	1.58	1.55	1.55	1.05	1.03	1.03	1.04	1.34	1.32	1.47	1.47
						Re = 1000						
65	0.124 179	0.121 146	—	—	0.782 128	0.783 456	—	—	0.457 776	0.470 430	—	—
129	0.051 978	0.051 735	0.046 169	0.046 380	0.544 739	0.546 456	0.565 525	0.568 647	0.230 639	0.238 365	0.338 832	0.340 169
257	0.017 065	0.017 048	0.016 146	0.016 222	0.256 228	0.257 526	0.280 737	0.284 390	0.081 443	0.084 864	0.153 368	0.153 689
α	1.60	1.60	1.51	1.51	1.08	1.08	1.01	0.99	1.50	1.48	1.14	1.14

TABLE VIII. Convergence of the LB simulations. The reference fields in Eq. (33) are obtained by using the PS-MG method with $N = 96$ collocation points in each dimension [18]. The PS-MG solutions are interpolated to the equispaced meshes used in the LB simulations. For the convergence speed α, "—" indicates the error not convergent, and "0" indicates very small α.

	$E_2(\boldsymbol{u})$				$E_2(\omega)$				$E_2(p)$			
N	MRT	TRT	ELBE	LBGK	MRT	TRT	ELBE	LBGK	MRT	TRT	ELBE	LBGK
						Re = 100						
65	0.009 656	0.009 596	0.013 264	0.012 407	0.404 343	0.403 632	0.405 224	0.411 644	0.139 478	0.132 741	0.130 186	0.130 833
129	0.004 881	0.004 762	0.006 520	0.004 521	0.349 975	0.348 526	0.341 324	0.348 427	0.142 614	0.126 274	0.108 636	0.107 584
257	0.002 627	0.002 536	0.007 008	0.005 103	0.312 173	0.310 392	0.309 956	0.318 039	0.139 070	0.118 188	0.210 484	0.209 649
513	0.001 230	0.001 159	0.008 170	0.006 575	0.278 520	0.276 377	0.317 375	0.325 069	0.133 328	0.110 153	0.294 257	0.293 612
α	1.09	1.12	—	—	0.16	0.16	—	—	0.06	0.10	—	—
						Re = 400						
65	0.014 338	0.013 976	0.032 697	0.032 139	0.537 835	0.538 175	0.577 239	0.582 646	0.059 236	0.064 428	0.552 563	0.557 939
129	0.005 045	0.005 046	0.011 319	0.010 116	0.434 750	0.435 049	0.450 761	0.456 535	0.060 323	0.064 410	0.215 502	0.217 022
257	0.002 425	0.002 412	0.005 523	0.003 001	0.358 009	0.357 551	0.356 791	0.362 463	0.065 658	0.063 101	0.063 333	0.063 627
513	0.001 103	0.001 076	0.004 624	0.001 022	0.299 231	0.298 099	0.292 251	0.297 964	0.067 925	0.061 149	0.054 081	0.053 463
α	1.13	1.16	0.25	0.28	0.25	0.26	0.28	0.28	—	0.045	0.22	0.25
						Re = 1000						
65	0.034 915	0.029 041	—	—	0.646 958	0.638 229	—	—	0.185 030	0.163 602	—	—
129	0.008 008	0.007 549	0.018 693	0.017 704	0.521 715	0.521 236	0.550 802	0.555 590	0.160 785	0.159 536	0.364 401	0.367 965
257	0.002 737	0.002 726	0.007 693	0.005 767	0.416 626	0.416 986	0.433 239	0.438 302	0.158 460	0.158 936	0.206 599	0.207 348
513	0.001 111	0.001 108	0.005 084	0.001 694	0.333 622	0.333 426	0.335 350	0.340 138	0.158 451	0.158 393	0.162 416	0.162 488
α	1.30	1.29	0.59	1.53	0.32	0.32	0.36	0.36	0	0.0049	0.34	0.35

grid refinement may not be negligible. The convergence speed α for the velocity field obtained by using the MRT-LB and TRT-LB schemes weakly depends on the Reynolds number Re: It varies between 1.09 at Re = 100 and 1.30 at Re = 1000. In contrast, the convergence speed of the velocity field obtained by using the ELBE and LBGK schemes has a much stronger dependence on Re. For both the ELBE and LBGK schemes, at Re = 100 the velocity field fails to converge. At Re = 400 and 1000, the ELBE scheme converges very slowly, while the LBGK scheme converges with a speed of about 1.5 or better. However, we can expect the convergence behavior of the ELBE and LBGK schemes to deteriorate as the mesh size N becomes sufficiently large that $\tau > 1$, due to their inaccurate BCs.

The vorticity field obtained by the LB schemes converges very slowly to the ps-mg solution, While the pressure field does not seem to converge at all. In absence of a body force, the vorticity $\boldsymbol{\omega}$ in compressible flows satisfies the following equation:

$$\partial_t \boldsymbol{\omega} + \boldsymbol{u}\cdot\nabla\boldsymbol{\omega} = \boldsymbol{\omega}\cdot\nabla\boldsymbol{u} - \boldsymbol{\omega}\nabla\cdot\boldsymbol{u} + \frac{1}{\rho^2}\nabla p \times \nabla p + \nabla \times \left(\frac{1}{\rho}\nabla\cdot\sigma\right), \tag{35}$$

where σ is the stress tensor including the bulk viscosity ζ. For incompressible flows, $\nabla\cdot\boldsymbol{u} = 0$, the density ρ is a constant, and the pressure p satisfies the Poisson equation. Since the LBE does not solve the Poisson equation accurately [29,51], the compressibility effect can affect $\boldsymbol{\omega}$ through all the terms involving $\boldsymbol{u}$, p, and σ in Eq. (35), because the velocity field $\boldsymbol{u}$ has a non-negligible dilatational component. It appears that the compressibility effect in the LB solution severely degrades the accuracy of the vorticity field in this case. We will quantify the compressibility effect later.

To further investigate the convergence behavior of the LB schemes, we compute the differences between the flow fields obtained by the LB schemes and the PS-MG method in the middle portion of the interior flow domain, which excludes $(N-1)/32$ grids around the boundary; this reduces the total number of grid points by about $N^2 \times 31/256 \approx N^2/8$. As shown in Table IX, the errors in the interior are significantly smaller than their counterparts on the entire flow domain Ω except the following cases: the velocity field computed by using the ELBE scheme at Re = 400 and 1000, the vorticity field by the ELBE and LBGK schemes at Re = 100, and the pressure field by all LB schemes at Re = 1000. The convergence speed is also changed. Compared to the errors on the entire flow domain Ω, the convergence speed of the velocity field by using the MRT-LB and TRT-LB schemes has decreases slightly to about 0.65 (from ca. 1.1), and has increases to about 1.68 and 1.81 (from ca. 1.13 and 1.30) at Re = 400 and 1000, respectively. The convergence speed obtained by using the ELBE scheme decreases to about 0.07 and 0.12 (from ca. 0.25 and 0.60) at Re = 400 and 1000, respectively, while that obtained by using the LBGK scheme decreases slightly to about 1.36 and 1.6 (from ca. 1.55 and 1.75).

The the convergence speed of ω on the interior flow domain is considerably better than that on the entire flow domain. It is particularly interesting to note that in many cases the convergence speed of the vorticity field ω in the interior flow domain is consistently better than that of the velocity field $\boldsymbol{u}$, as evidently shown in Table IX. For the MRT-LB and TRT-LB schemes, the convergence speed of ω is better than 1.9 in all cases, as opposed to between 0.16 and 0.32 on the entire flow domain. The ability of the MRT-LBE to accurately compute vorticity field has also been observed in simulations

TABLE IX. Convergence of the LB simulations, same as in Table VIII. The errors are computed over the interior flow domain by cutting away $(N-1)/32$ grid points along the boundary. For the convergence speed α, "—" indicates the error not convergent, and "0" indicates very small α.

	$E_2(\boldsymbol{u})$				$E_2(\omega)$				$E_2(p)$			
N	MRT	TRT	ELBE	LBGK	MRT	TRT	ELBE	LBGK	MRT	TRT	ELBE	LBGK
Re = 100												
65	0.003 252	0.003 191	0.005 719	0.004 002	0.035 406	0.037 472	0.082 058	0.083 648	0.014 485	0.014 595	0.062 072	0.062 115
129	0.000 779	0.000 767	0.003 543	0.000 608	0.011 840	0.012 174	0.014 103	0.013 633	0.011 412	0.011 346	0.011 463	0.011 121
257	0.000 238	0.000 238	0.003 459	0.000 874	0.003 290	0.003 324	0.007 181	0.001 070	0.010 858	0.010 839	0.012 035	0.011 690
513	0.000 152	0.000 152	0.003 462	0.001 010	0.000 868	0.000 869	0.008 341	0.003 268	0.010 733	0.010 728	0.012 277	0.011 936
α	0.65	0.65	—	—	1.92	1.93	—	—	0.0016	0.0014	—	—
Re = 400												
65	0.012 047	0.011 806	0.018 762	0.017 260	0.061 100	0.055 325	0.294 266	0.297 101	0.040 048	0.038 949	0.366 186	0.368 029
129	0.002 522	0.002 508	0.005 850	0.001 903	0.016 072	0.015 879	0.040 473	0.039 531	0.035 796	0.035 834	0.046 303	0.045 871
257	0.000 577	0.000 580	0.004 789	0.000 434	0.004 224	0.004 235	0.010 929	0.005 740	0.035 835	0.035 792	0.036 286	0.035 842
513	0.000 180	0.000 181	0.004 563	0.000 169	0.001 107	0.001 107	0.008 579	0.001 189	0.035 868	0.035 850	0.036 271	0.035 855
α	1.68	1.68	0.0069	1.36	1.93	1.93	0.34	2.27	—	—	0	—
Re = 1000												
65	0.034 225	0.028 946	—	—	0.114 977	0.103 268	—	—	0.191 773	0.186 110	—	—
129	0.006 475	0.006 042	0.007 961	0.004 135	0.028 005	0.026 225	0.133 858	0.134 461	0.178 741	0.178 870	0.210 671	0.210 918
257	0.001 408	0.001 388	0.005 462	0.000 653	0.006 668	0.006 636	0.016 632	0.009 163	0.178 174	0.178 190	0.178 190	0.178 197
513	0.000 401	0.000 402	0.005 028	0.000 215	0.001 722	0.001 722	0.012 118	0.001 900	0.178 148	0.178 144	0.178 118	0.178 141
α	1.81	1.78	0.11	1.60	1.95	1.94	0.45	2.26	0	0	0	0

of turbulence in three dimensions [16]. For the LBGK scheme, the convergence speed of ω is better than 2.2 at $\mathrm{Re} = 400$ and 1000. As for the ELBE scheme, the convergence speed of ω is only 0.34 and 0.45 at $\mathrm{Re} = 400$ and 1000, respectively. As for the pressure field p, the convergence speed remains the same as on the entire flow domain; the pressure field does not appear to converge to the PS-MG solution.

The data in Table IX reveal some interesting observations. First, the error in the LB simulations concentrates mostly in the boundary region. In the case of the cavity flow, the corner singularities may be the main cause of the problem. Secondly, with carefully tuned equilibria, the MRT-LBE can solve both the velocity field $\boldsymbol{u}$ and vorticity field ω with a convergence speed about 2 in regions where the flow is smooth. This can be explained as the following. According to Noether's theorem, which states that any differentiable symmetry of the action of a physical system has a corresponding conservation law, the conservation laws of the linear and angular momenta correspond to Galilean and rotational invariance, respectively. The LBE preserves both invariances up to second order in the wave vector $\boldsymbol{k}$ [9] and consequently the conservation laws of the linear and angular momenta to the same order of accuracy. Although this does not constitute a rigorous proof, it helps explain the phenomenon.

With $\mathrm{Ma} = 0.1 \times \sqrt{3} \approx 0.1732$, the rms density fluctuation $\sqrt{\langle \delta\rho^2 \rangle}$ in the system is of the order $O(10^{-3})$ (cf. Table X related discussion later). Given the fact that the pressure field p obtained by using the LB schemes has a significant compressibility component proportional to Ma^2, it is expected that the pressure p is most sensitive to the error due to the compressibility effect in the LBE. The data in Table IX attest again the crucial role that the BCs play in the LB simulations. Clearly, the MRT-LB and TRT-LB schemes are far more accurate than the ELBE and LBGK schemes in terms of the convergence speed and the magnitude of errors in $\boldsymbol{u}$ and ω, and the ELBE scheme is the most inferior in all these measures.

To quantify the compressibility effect, we compute the rms density fluctuation $\sqrt{\langle (\delta\rho)^2 \rangle}$ and the rms velocity divergence $\sqrt{\langle (\boldsymbol{\nabla} \cdot \boldsymbol{u})^2 \rangle}$ in the system

$$\sqrt{\langle (\delta\rho)^2 \rangle} = \left[\frac{\sum_i (\delta\rho)^2(\boldsymbol{x}_i)}{N_x N_y} \right]^{1/2}, \tag{36a}$$

$$\sqrt{\langle (\boldsymbol{\nabla} \cdot \boldsymbol{u})^2 \rangle} = \left[\frac{\sum_i (\boldsymbol{\nabla} \cdot \boldsymbol{u})^2(\boldsymbol{x}_i)}{N_x N_y} \right]^{1/2}, \tag{36b}$$

where $\boldsymbol{x}_i$ are fluid nodes. The results of $\sqrt{\langle (\delta\rho)^2 \rangle}$ and $\sqrt{\langle (\boldsymbol{\nabla} \cdot \boldsymbol{u})^2 \rangle}$ are tabulated in Table X.

Several observations can be made. First of all, for all LB schemes, with a fixed the Mach number Ma, the rms density fluctuation $\sqrt{\langle (\delta\rho)^2 \rangle}$ is nearly independent of the mesh resolution N and decreases as the Reynolds number Re increases. The rms density fluctuation is approximately equal to 3.0×10^{-3}, 1.6×10^{-3}, and 1.3×10^{-3} at $\mathrm{Re} = 100$, 400, and 1000, respectively.

Second, for the MRT-LB and TRT-LB schemes, the rms velocity divergence $\sqrt{\langle (\boldsymbol{\nabla} \cdot \boldsymbol{u})^2 \rangle}$ does not seem to depend on either N or Re. As for the ELBE and LBGK schemes, the rms velocity divergence decreases as N increases and increases as Re increases. Since in the ELBE and LBGK schemes the bulk viscosity $\zeta = \nu/2$, as Re increases with a fixed N, ζ decreases, and so similarly do the decay rates of all other nonconserved modes, leading to weaker dissipation to all nonconserved

TABLE X. The dependence of the rms density fluctuation $\sqrt{\langle(\delta\rho)^2\rangle}$ and the rms velocity divergence $\sqrt{\langle(\boldsymbol{\nabla}\cdot\boldsymbol{u})^2\rangle}$ on the Reynolds number Re and the mesh size N.

	rms density fluctuation				rms velocity divergence			
N	MRT	TRT	ELBE	LBGK	MRT	TRT	ELBE	LBGK
				Re = 100				
65	0.002 569	0.002 574	0.002 850	0.002 855	0.305 216	0.302 737	0.360 637	0.361 507
129	0.002 753	0.002 764	0.002 789	0.002 793	0.305 982	0.299 739	0.309 758	0.310 092
257	0.002 926	0.002 940	0.002 803	0.002 806	0.309 262	0.298 951	0.241 936	0.239 084
513	0.003 091	0.003 105	0.002 822	0.002 826	0.313 143	0.298 658	0.191 387	0.181 124
				Re = 400				
65	0.001 533	0.001 530	0.001 898	0.001 905	0.321 806	0.329 121	0.530 087	0.528 835
129	0.001 564	0.001 563	0.001 670	0.001 672	0.310 099	0.311 752	0.426 615	0.428 021
257	0.001 586	0.001 587	0.001 618	0.001 619	0.305 285	0.302 858	0.359 677	0.362 329
513	0.001 607	0.001 608	0.001 610	0.001 611	0.305 859	0.299 648	0.308 708	0.310 513
				Re = 1,000				
65	0.001 321	0.001 329	—	—	0.345 939	0.359 265	—	—
129	0.001 368	0.001 368	0.001 491	0.001 491	0.325 027	0.334 810	0.567 532	0.567 025
257	0.001 379	0.001 379	0.001 413	0.001 411	0.313 045	0.316 334	0.456 678	0.458 426
513	0.001 384	0.001 384	0.001 396	0.001 394	0.305 985	0.304 804	0.375 882	0.379 374

modes, including the modes related to the compressibility term $\boldsymbol{\nabla}\rho\zeta\boldsymbol{\nabla}\cdot\boldsymbol{u}$ in the Navier-Stokes equation. In the case of increasing N with a fixed Re, ζ and all the other decay rates increase, resulting in stronger dissipation to the modes related to the compressibility effect. This explains the dependence of the rms velocity divergence on N and Re for the ELBE and LBGK schemes. It is interesting to note that the bulk viscosity ζ in the MRT-LBE is fixed, while in the TRT-LBE it is identical to that in the LBGK scheme, and yet, the rms density fluctuation and the rms velocity divergence behave almost identically for the MRT-LB and TRT-LB schemes. This indicates that the dissipation of the "heat fluxes" $\boldsymbol{q}$, determined by s_q, and the BCs play a crucial role here. This is certainly more complicated than the case without boundary [23] and suggests that the TRT-LBE is a much better approach than the ELBE with a tunable bulk viscosity [26].

Finally, since the rms density fluctuation and the rms velocity divergence are the direct measures of the compressibility effect, which is proportional to $O(\mathrm{Ma}^2)$, and the pressure field is most direly affected by the compressibility effect through the simple equation of state in the LBE, $p = c_s^2\rho$, to improve the accuracy of the pressure field p, the Mach number must be decreased, as observed previously (cf. [23,43]).

TABLE XI. The values of the relaxation rates used in the stability test shown in Fig. 13.

	Relaxation rates		
Model	s_e	s_ε	s_q
MRT	1.64	1.54	$8(2\tau-1)/(8\tau-1)$
MRT1	1.64	1.54	1.9
MRT2	1.8	1.54	1.9
MRT3	1.64	1.8	1.9
MRT4	$1/\tau$	1.9	$8(2\tau-1)/(8\tau-1)$
TRT	$1/\tau$	$1/\tau$	$8(2\tau-1)/(8\tau-1)$

E. Stability and computational efficiency

To compare the numerical stability of the LB schemes, we conduct the following test. With a small mesh size $N^2 = 17^2$ and a given value of the viscosity ν, we search the maximum lid velocity U such that the simulation does not diverge with 1000 iterations. For the MRT-LBE, in addition to $s_\nu = 1/\tau$, there are three adjustable relaxation rates: s_q, s_e, and s_ϵ. To accurately realize the no-slip BCs through the BB BCs, s_q must be a fixed function of s_ν [cf. Eq. (11)]. However, to demonstrate the effect of s_q on the numerical stability of the MRT-LBE, we also vary s_q independently in the test. Table XI lists the values of relaxation rates used in the test.

In Fig. 13 we show the result of the stability test. Clearly, the ELBE and LBGK schemes are shown to be the most inferior in this test, and there is no observable difference between the ELBE and the LBGK schemes in terms of stability. It is evident that the ELBE scheme does not improve numerical stability of the LBGK scheme. The TRT-LB scheme is more

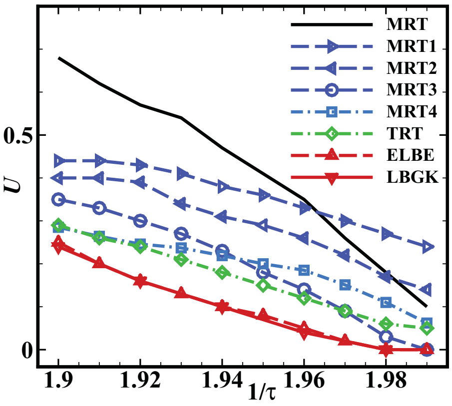

FIG. 13. (Color online) The stability characteristics of various LBE models. $N^2 = 17^2$. The test is deemed stable if it does not diverge within 1000 iterations.

TABLE XII. The number of iterations N_t and CPU time T_{CPU} (seconds) for different LB schemes to attain the steady state with different values of the Reynolds number Re. $N^2 = 129^2$. The numbers in parentheses are the ratio R_{T} of the CPU times of the TRT, MRT, and ELBE schemes *vs.* that of the LBGK scheme. "—" indicates the simulation does not converge.

	1000			1500			1800			2000	
Re	N_t	T_{CPU}	R_{T}	N_t	T_{CPU}	R_{T}	N_t	T_{CPU}	R_{T}	N_t	T_{CPU}
LBGK	413 000	194.12	(1)	645 000	296.11	(1)	785 000	354.63	(1)	—	
TRT	413 000	217.77	(1.12)	643 000	338.75	(1.14)	782 000	413.48	(1.17)	874 000	460.34
MRT	413 000	235.96	(1.22)	645 000	366.74	(1.24)	785 000	443.76	(1.25)	878 000	498.29
ELBE	415 000	491.39	(2.53)	648 000	766.60	(2.59)	790 000	930.06	(2.62)	—	

stable than both the ELBE and the LBGK schemes. By far, the MRT-LBE is the most stable scheme. However, as the viscosity ν decreases, the stability of the MRT-LB scheme deteriorates considerably. As $s_\nu = 1/\tau$ approaches to 2, $s_q(s_\nu)$ approaches 0, and the relaxation time of the modes q_x and q_y becomes longer and longer, so that q_x and q_y become quasiconserved modes eventually when s_q is sufficiently small. This apparently affects the stability of the MRT-LBE when $s_\nu = 1/\tau$ is close to 2. If s_q is fixed at 1.9 or so while other relaxation rates are unchanged (corresponding to MRT1 in Table XI and Fig. 13), then the stability of the MRT-LBE is improved when $s_\nu = 1/\tau \gtrsim 1.965$, but degraded when $s_\nu = 1/\tau \lesssim 1.965$, as shown in Fig. 13. If we use $s_q = 1.9$ and increase s_e from 1.64 to 1.8 (the case MRT2 in Fig. 13), the stability is weaker than the case of MRT1.

We note that the numerical stability of the LBE can be affected by factors other than the relaxation rates. For example, the stability would be different if one uses the "compressible" version of the LBGK model of which the equilibria are [52]

$$f_i^{(\mathrm{eq})} = w_i\, \rho \left[1 + \frac{\boldsymbol{c}_i \cdot \boldsymbol{u}}{c_s^2} + \frac{1}{2} \left\{ \frac{(\boldsymbol{c}_i \cdot \boldsymbol{u})^2}{c_s^4} - \frac{\boldsymbol{u} \cdot \boldsymbol{u}}{c_s^2} \right\} \right]. \tag{37}$$

We do not use the compressible LB model because we would like to minimize the compressibility effect, because we are only interested in simulating incompressible flows. Another factor may be the mean density ρ_0. In our implementation, we set $\rho_0 = 1$ so the LBE can approximate the Poisson equation obeyed by the pressure [51]. In addition, to reduce the effects due to round-off error we only consider the density fluctuation $\delta\rho$ in the mass conservation [22,23], as indicated in the equilibria defined by Eqs. (5) and (12). With a value of $\rho_0 > 1$ [52], the effect of the round-off error is enhanced, but the relative density fluctuation $\delta\rho/\rho_0$ is reduced; hence, the stability might be improved.

We should also emphasize that the numerical stability must be discussed in connection with accuracy and computational efficiency. That is, one must not pursue stability at the expense of accuracy and efficiency, and especially accuracy. To optimize the computational efficiency, U should be maximized, for a larger U effectively leads to a larger CFL number, as discussed previously in Sec. III A. However, the truncation error due to $\boldsymbol{u}^3$ terms grows as U increases [9], which can be eliminated only with a larger discrete velocity set, for example, D2Q21 model [53]. With these considerations in mind, one should use the maximal value of U without compromising accuracy. With U properly chosen, the issue of optimizing the stability becomes minimizing the viscosity ν. However, one should not relentlessly push the lower limit of ν; otherwise, the results of direct numerical simulations become dubious if the grid Reynolds number $\mathrm{Re}^* := U\delta_x/\nu$ becomes too large. Thus, one must strike a balance between accuracy, efficiency, and stability, and in that order.

To compare the computational speed of different LB schemes, we use a mesh of size $N^2 = 129^2$ with the Reynolds numbers Re = 1000, 1500, 1800, and 2000. All the computations are carried out on an Intel Xeon (x86-64) processor with two dual cores of 2.992 GHz and 8 GB RAM. The codes are written in C and compiled with the Intel compiler ICPC. Table XII provides the number of iterations (N_t) and the CPU times (T_{CPU}) for the LB schemes to attain a steady state according to the criterion of Eq. (21), and the ratios (R_{T}) between the CPU times of the MRT, TRT, and ELBE schemes versus the LBGK scheme, of which the CPU time is the shortest. Clearly, we can see in Table XII that the number of iterations to reach steady state $N_t \propto N\mathrm{Re}/U$. The results also show that, while the TRT-LB and MRT-LB schemes are about 15% and 25% slower than the LBGK scheme in terms of CPU time, respectively, the ELBE scheme is about 2.5 times slower. We also note that with the mesh size of $N^2 = 129^2$, both the ELBE and the LBGK do not converge for $Re = 2000$.

IV. CONCLUSIONS AND DISCUSSION

In this work we conduct a comparative study of several lattice Boltzmann schemes including the MRT-LB, TRT-LB, ELBE, and LBGK D2Q9 models, in terms of accuracy, numerical stability, and computational efficiency. As a benchmark test, we use the lid-driven square cavity flow in 2D with the Reynolds numbers Re = 100, 400, and 1000, for which the flow is steady and laminar. We compare the LB solutions with the solutions obtained by using the PS-MG method with singularity subtraction technique [18]. The evidence shows that the MRT-LB and TRT-LB schemes are superior over the ELBE and LBGK schemes in terms of accuracy, stability, and computational efficiency.

We made the following observations through this study. First, all the LB schemes are capable of capturing the gross hydrodynamic features of the flow. We compare the contours of the pressure field p, the stream function ψ, and the vorticity field ω computed by using the LB schemes with those by using the PS-MG method [18] and find that they agree well with each other. The LB schemes can reproduce quantitatively accurate results, such as the locations and intensities of the primary, secondary, and even tertiary vortices. Both the MRT-LB and the TRT-LB schemes can capture the tertiary vortex at $\mathrm{Re} = 1000$ with a mesh of size $N^2 = 129^2$, while both the ELBE and LBGK schemes require a finer mesh of size $N^2 = 257^2$ to observe the tertiary vortex.

Second, we observe that one major source of errors in the LB simulations comes from BCs, and this problem is particularly severe for the ELBE and LBGK schemes coupled with the BB BCs. The problem is twofold: With the relaxation parameter τ close to $1/2$, flow fields near no-slip boundaries oscillate severely with high frequencies, and with $\tau \gg 1$, the boundary locations move away from supposed positions considerably and are τ dependent. Both these defects can be overcome by using the MRT models.

Third, all the LB schemes (MRT, TRT, ELBE, and LBGK) exhibit a self-consistent convergence behavior of a second-order scheme, as expected [29]. The solutions of the velocity $\boldsymbol{u}$, the vorticity ω, and the pressure p obtained by using a particular LB scheme converge to unique limiting states as the resolution N increases with expected convergence speed. However, the LB solutions of $\boldsymbol{u}$, ω, and p do not necessarily converge to the corresponding solutions of the PS method [18]. When compared with the PS solution of the velocity field $\boldsymbol{u}$ on the entire flow domain, both the MRT-LB and TRT-LB schemes are shown to be only marginally of second-order convergence, so is the LBGK scheme at $\mathrm{Re} = 1000$, while the ELBE scheme is only of first-order. However, when compared with the PS solution of the velocity field $\boldsymbol{u}$ in the interior flow domain, the MRT-LB, TRT-LB, and LBGK schemes are clearly of second-order convergence, and the ELBE scheme is only of first-order convergence, except for the case of $\mathrm{Re} = 100$. At $\mathrm{Re} = 100$, both the MRT-LB and the TRT-LB schemes are of first-order convergence, while neither the ELBE scheme nor the LBGK scheme converges at all. In particular, it is interesting to note that the vorticity field obtained by using the MRT-LB and TRT-LB schemes, and the LBGK scheme in some cases, is of second-order convergence, and the convergence speed is consistently better than that of the velocity field, while the convergence speed for the ELBE is only of first-order. In most cases, the pressure field p obtained by the LB schemes either converges very slowly or does not converge at all to the PS solution.

Fourth, we note that the ELBE scheme does not in any way improve the stability of the LBGK scheme, while its computational cost is almost tripled. In terms of accuracy, the ELBE scheme is even inferior to the LBGK scheme. One reason that the ELBE cannot improve the stability is that, when τ is approaching $1/2$, the ELBE does not have sufficient dissipation to damp density fluctuations in the system [9], and the interactions of the acoustic waves generated by density fluctuations can instigate numerical instabilities. To overcome this shortcoming of the ELBE scheme, an adjustable bulk viscosity can be introduced [26]. This approach basically adopts the MRT technique, but only half-heartily, while clinging to all other deficiencies inherent to the ELBE/SRT methodology. We do not test the ELBE with a variable relaxation time [52,54], which is supposed to guarantee numerical stability, because it is computationally inefficient and unphysical with a viscosity depending on space and time; a stable but inaccurate, unphysical, and inefficient scheme is simply not a viable one.

Fifth, in terms of CPU time the LBGK scheme is only about 25% and 15% faster than the MRT and TRT schemes, respectively. However, given the inherent deficiencies in the LBGK scheme, this insignificant saving in CPU time is beside the point, because the LBGK scheme with the BB BCs cannot yield convergent results as the mesh size N increases. Furthermore, for most LB algorithms which are light in floating point operations (FLOPs), the computational speed is limited by memory bandwidth and cache size; thus, the difference in the computational speed due to insignificantly different number of FLOPs will diminish. Thus, 25% difference in CPU time is not a valid justification to promote the LBGK scheme.

Finally, we would like to discuss the choice of the relaxation rates $\{s_i\}$ in the MRT-LBE. Often, critics of the MRT methodology complain about its "complexity," and one aspect of the complexity is that it appears that there are no analytic guidelines to determine the relaxation rates. These criticisms are not entirely valid. First of all, the MRT collision model is a *linear* one, of which the LBGK model is a special case, and it is well understood in kinetic theory and there exists a vast literature on the subject (cf., e.g., [21] and references therein).

Within the context of the LBE, certain guidelines do exist. In kinetic theory, hydrodynamic time scales of the conserved modes are vastly separated from those of kinetic (nonconserved) modes, that is, time scales of kinetic (non-conserved) modes are much shorter than the hydrodynamic ones. This vast separation of time scales is not satisfied in the LBE for it has very limited number of modes which are closely coupled together through relative simple algebraic relationships defined by the LBE (2), so the range of these relaxation rates is rather limited, and the dynamics of kinetic modes in the LBE has severe effects on BCs and numerical stability. It is difficult to determine, analytically and *a priori*, optimal relaxation rates in terms of both accuracy and stability. This is especially true for 3D models with a large number of discrete velocities (or the moments).

While it is relatively easy to obtain relaxation rates for optimal *linear* stability [9], it is not so for *nonlinear* stability. It is also not easy to analytically determine the effects of relaxation rates on the BCs in general (cf. [14]). However, one can still determine the relaxation rates which can be used to yield reasonable accuracy and stability. In this regard, the TRT-LBE is the simplest alternative which improves both accuracy and numerical stability. The point to emphasize is that the MRT formalism allows improvements by adjusting the relaxation rates, which is not possible for the models with SRT. We note that a thorough and detailed investigation of the effects of the relaxation rates on the accuracy and stability is beyond the scope of this work and should be a subject of future studies.

The results of this study demonstrate that there are at least three relaxation rates, s_ν, s_q, and s_e, which have significant effects on accuracy and numerical stability of the MRT-LBE. Therefore, to optimize accuracy and numerical stability, it is necessary to have three adjustable degrees of freedom in the MRT-LBE provided by s_ν, s_q, and s_e, which determine the value of the shear viscosity ν (or the Reynolds number Re), the accurate locations of the Dirichlet BCs, and the bulk viscosity ζ [cf. Eq. (10b)]. If numerical stability is not a consideration, one should use the TRT-LBE [5–7]; that is, the odd-order moments are relaxed by the rate $s_q(s_\nu)$ (cf., e.g., Eq. (11) and [14,55] and references therein), while the even-order moments are relaxed with the rate s_ν. With three adjustable relaxation rates, the MRT-LBE provides minimal degrees of freedom required by accuracy and stability, and can enhance the computational efficiency ultimately.

In summary, our conclusion is that, while it may be theoretically interesting, the ELBE scheme is so inferior to the MRT scheme in terms of accuracy, numerical stability, and computational efficiency that it must not be used as a practical scheme for numerical simulations. We also note that one important and challenging issue in the LBE is to improve accuracy of the pressure field p. In this regard, investigation of the artificial compressibility method [31,32] may offer some new insights.

ACKNOWLEDGMENTS

This work is supported by the National Science Foundation (NSF) of the United States through Grant No. DMS-0807983. L.S.L. would like to acknowledge the support of the Richard F. Barry Jr. endowment at the Old Dominion University (ODU) and support from the Isaac Newton Institute of Mathematical Sciences, University of Cambridge, UK. X.W.C. would like to acknowledge the generous support of the Modeling and Simulation Program provided by ODU during 2008–2010. L.S.L. is grateful to Drs. Pierre Lallemand and Dominique d'Humières for insightful discussions and suggestions.

---

[1] R. Mei, D. Yu, W. Shyy, and L.-S. Luo, Phys. Rev. E **65**, 041203 (2002).
[2] L.-S. Luo, M. Krafczyk, and W. Shyy, in *Encyclopedia of Aerospace Engineering*, edited by R. Blockley and W. Shyy (Wiley, New York, 2010), Chap. 56, pp. 651–660.
[3] S. Ansumali, I. V. Karlin, and H. C. Öttinger, Europhys. Lett. **63**, 798 (2003).
[4] S. Succi, I. V. Karlin, and H. Chen, Rev. Mod. Phys. **74**, 1203 (2002).
[5] I. Ginzburg, Adv. Water Res. **28**(11), 1171 (2005).
[6] I. Ginzburg, F. Verhaeghe, and D. d'Humières, Comput. Phys. Commun. **3**, 427 (2008).
[7] I. Ginzburg, F. Verhaeghe, and D. d'Humières, Comput. Phys. Commun. **3**, 519 (2008).
[8] D. d'Humières, in *Rarefied Gas Dynamics: Theory and Simulations*, Vol. 159 of Progress in Astronautics and Aeronautics, edited by B. D. Shizgal and D. P. Weave (AIAA, Washington, DC, 1992), pp. 450–458.
[9] P. Lallemand and L.-S. Luo, Phys. Rev. E **61**, 6546 (2000).
[10] D. d'Humières, I. Ginzburg, M. Krafczyk, P. Lallemand, and L.-S. Luo, Philos. Trans. R. Soc. London A **360**, 437 (2002).
[11] P. Lallemand and L.-S. Luo, Phys. Rev. E **68**, 036706 (2003).
[12] X. He and L.-S. Luo, Phys. Rev. E **55**, R6333 (1997).
[13] X. He and L.-S. Luo, Phys. Rev. E **56**, 6811 (1997).
[14] I. Ginzburg and D. d'Humières, Phys. Rev. E **68**, 066614 (2003).
[15] C. Pan, L.-S. Luo, and C. Miller, Comput. Fluids **35**, 898 (2006).
[16] Y. Peng, W. Liao, L.-S. Luo, and L.-P. Wang, Comput. Fluids **39**, 568 (2010).
[17] O. Botella and R. Peyret, Comput. Fluids **27**, 421 (1998).
[18] W. Zhang, C. Zhang, and G. Xi, Comput. Fluids **39**, 178 (2010).
[19] L.-S. Luo, Comput. Phys. Commun. **129**, 63 (2000).
[20] Y. Qian, D. d'Humières, and P. Lallemand, Europhys. Lett. **17**, 479 (1992).
[21] S. Harris, *An Introduction to the Theory of Boltzmann Equation* (Holt, Rinehart, and Winston, New York, 1971; reprinted by Dover, New York, 2004).
[22] X. He and L.-S. Luo, J. Stat. Phys. **88**, 927 (1997).
[23] P. Dellar, J. Comput. Phys. **190**, 351 (2003).
[24] I. Ginzbourg, Ph.D. thesis, Universite Paris VI, France, 1994.
[25] I. Ginzbourg and P. M. Adler, J. Phys. II **4**, 191 (1994).
[26] P. Asinari and I. V. Karlin, Phys. Rev. E **81**, 016702 (2010).
[27] W.-A. Yong and L.-S. Luo, Phys. Rev. E **67**, 051105 (2003).
[28] W.-A. Yong and L.-S. Luo, J. Stat. Phys. **121**, 91 (2005).
[29] M. Junk, A. Klar, and L.-S. Luo, J. Comput. Phys. **210**, 676 (2005).
[30] L. Saint-Raymond, *Hydrodynamic Limits of the Boltzmann Equation*, Vol. 1971 of Lecture Notes in Mathematics (Springer, Heidelberg, Germany, 2009).
[31] P. Asinari and V. Karlin, Comput. Math. Appl. **58**, 841 (2009).
[32] T. Ohwada and P. Asinari, J. Comput. Phys. **229**, 1698 (2010).
[33] L.-S. Luo, J. Stat. Phys. **88**, 913 (1997).
[34] X. He, Q. Zou, L.-S. Luo, and M. Dembo, J. Stat. Phys. **87**, 115 (1997).
[35] S. Ansumali, I. Karlin, C. Frouzakis, and K. Boulouchos, Physica A **359**, 289 (2006).
[36] Y. Zhou, R. Zhang, I. Staroselsky, H. Chen, W. Kim, and M. Jhon, Physica A **362**, 68 (2006).
[37] J. Ghazanfarian and A. Abbassi, Phys. Rev. E **82**, 026307 (2010).
[38] C. Shen, D. B. Tian, C. Xie, and J. Fan, Microscale Thermophys. Eng. **8**, 423 (2004).
[39] L.-S. Luo, Phys. Rev. Lett. **92**, 139401 (2004).
[40] R. Rubinstein and L.-S. Luo, Phys. Rev. E **77**, 036709 (2008).
[41] F. Verhaeghe, L.-S. Luo, and B. Blanpain, J. Comput. Phys. **228**, 147 (2009).
[42] U. Ghia, K. N. Ghia, and C. T. Shin, J. Comput. Phys. **48**, 387 (1982).
[43] S. L. Hou, Q. Zou, S. Chen, G. D. Doolen, and A. C. Cogley, J. Comput. Phys. **118**, 329 (1995).
[44] P. Shankar and M. Deshpande, Annu. Rev. Fluid Mech. **32**, 93 (2000).
[45] C.-H. Bruneau and M. Saad, Comput. Fluids **35**, 326 (2006).
[46] G. Zanetti, Phys. Rev. A **40**, 1539 (1989).
[47] R. Brito and M. Ernst, J. Phys. A **24**, 3331 (1991).
[48] D. P. Lockard, L.-S. Luo, S. D. Milder, and B. A. Singer, J. Stat. Phys. **107**, 423 (2002).
[49] C. K. Aidun and J. R. Clausen, Annu. Rev. Fluid Mech. **42**, 439 (2010).
[50] L.-S. Luo, Phys. Rev. E (unpublished).
[51] R. Mei, L.-S. Luo, P. Lallemand, and D. d'Humières, Comput. Fluids **35**, 855 (2006).
[52] F. Tosi, S. Ubertini, S. Succi, and V. Karlin, J. Sci. Comput. **30**, 369 (2007).
[53] P. Philippi, L. Hegele, L. dos Santos, and R. Surmas, Phys. Rev. E **73**, 056702 (2006).
[54] S. Ansumali and I. V. Karlin, Phys. Rev. E **65**, 056312 (2002).
[55] F. Dubois, P. Lallemand, and M. Tekitek, Comput. Math. Appl. **59**, 2141 (2009).